Liquid Argon Scintillation Light Quenching due to Nitrogen Impurities: Measurements performed for the MicroBooNE Vertical Slice Test

by

Christie Shinglei Chiu

Submitted to the Department of Physics
in partial fulfillment of the requirements for the degree of

Bachelor of Science in Physics

at the

MASSACHUSETTS INSTITUTE OF TECHNOLOGY

June 2013

Author .....
Department of Physics
May 10, 2013

Certified by .....
Janet M. Conrad
Professor of Physics, Department of Physics
Thesis Supervisor

Accepted by .....
Nergis Mavalvala
Senior Thesis Coordinator, Department of Physics

Liquid Argon Scintillation Light Quenching due to Nitrogen Impurities: Measurements performed for the MicroBooNE Vertical Slice Test

by

Christie Shinglei Chiu

Submitted to the Department of Physics
on May 10, 2013, in partial fulfillment of the
requirements for the degree of
Bachelor of Science in Physics

Abstract

The neutrino experiment MicroBooNE is currently under construction. To expedite the physics output of MicroBooNE, a smaller version of its optical detection system has been implemented. To demonstrate full operability of this prototype, two physics measurements were performed. The first examines the number of scintillation light components, for although theory explains two components, other groups have seen evidence for a third. The second measures late light quenching as a function of nitrogen gas impurity concentration in the liquid argon. We find marginal evidence for a third component and further steps are identified to improve upon this study. Our late light quenching measurement also agrees with previously published results in the literature. These two measurements are useful not only from a detector development standpoint, but also for detector simulations.

Thesis Supervisor: Janet M. Conrad
Title: Professor of Physics, Department of Physics

Acknowledgments

I could not have wished for a better undergraduate experience. I've always wanted to come to MIT, but it wasn't until I actually got here that I realized what a special place it is. Here, you are pushed to your limits- not only in academics, but also in research, leadership, and extracurriculars- and not because of competition between your peers, because MIT's not like that. It's because everyone around you- professors, research advisors, classmates, and administrators- knows what great achievements of which you are capable.

Much of what made these past few years so fantastic was the research, and I have Professor Janet Conrad to thank for this. Never did I imagine that I would find such an enthusiastic advisor who truly looks out for her research group and provides them with the best opportunities possible, and that she would take me into her group as an undergraduate. From coaching me through my first first-author paper to sending me to Fermilab for my summer UROP, Janet's been wholeheartedly supportive, utterly inspirational, and downright instrumental in my development as an experimental physicist, and I can never thank her enough for that.

Many thanks also to Christina Ignarra, Ben Jones, and the rest of our wonderful group; they all have been enormously welcoming, and they make it very difficult for me to leave next year. Christina was always there to help me out when I was just starting out and completely lost, whether it be obtaining new glassware for the TPB coatings, teaching me how to use new equipment, or even just turning on the deuterium light source every morning so that it was ready to go when I went to take data in the afternoons.

I am tremendously grateful to Ben for the incredible amount of work he did in preparation for my UROP this past summer, and especially for my thesis work over IAP. Both times, he made sure that all of the necessary hardware was perfectly in place for me to begin research right away, even when this involved working with who knows how many groups to install an entirely new system. He contributed essentially his entire January helping me with my thesis work, including developing

the deconvolution analysis method mentioned in chapter 4 and creating many of the figures. Ben provided the perfect medium between assisting me in my work and giving me the freedom to stuggle in solving problems, which is no easy task.

UROP at MIT has really made this all possible, and it is a truly fantastic program[1]. If you are an MIT undergraduate reading this and you don't have a UROP, stop reading and get one. Now. I hear Janet Conrad's a really good professor to work with!

Thank you also to Professor Martin Zwierlein, whose animated teaching of 8.012 gave me a beautiful introduction to MIT and its physics department. He gave me a new appreciation for physics and sparked my interest to learn more, and I hope that one day I will be a professor who inspires students to pursue physics as he has done for me.

Of course I must thank Professor Nergis Mavalvala, whose unending patience eased the growing pains of Junior Lab. Her cheery smile and caring eyes calmed my nerves when I went to give each JLab presentation, to the point where by the end of the semester, I really enjoyed giving talks. Nergis taught me how to be more inquisitive and analytical in the lab, and showed me how to be a good mentor as a teaching assistant my senior year.

Finally, I am forever indebted to my parents, Steve and Michell Chiu, and my brother, Michael Chiu. They have always supported me- financially, nutritionally, emotionally, and more- and they have always told me that I could accomplish anything I wanted. I thank them for allowing me to dream big when I was little, for celebrating with me in my successes, and for consoling me in my failures. I have the best family ever.

[1]Acknowledgements also to the National Science Foundation; this research is supported by NSF-PHY-1205175.

Contents

List of Figures

Chapter 1

Introduction

"I have done a terrible thing. I invented a particle that cannot be detected."

- Wolfgang Pauli

Since its postulated existence by Wolfgang Pauli in 1930, the neutrino has always been known to be an elusive particle. Indeed, neutrinos are the most weakly interacting particles of the elementary particles currently known to physicists, which makes learning their properties exceedingly difficult. It took 26 years to even achieve detection of this particle, accomplished by Clyde Cowan and Frederick Reines. In the decades since, physicists have developed many technologies to learn much about its nature. In particular, a new generation of neutrino detectors called liquid argon time projection chambers (LArTPCs) allow for high-resolution particle tracking and measurements of energy deposition along each track. Thus, LArTPCs are well-equipped to measure neutrino oscillation parameters and resolve the neutrino mass hierarchy. Previous such detectors include ICARUS [1] and ArgoNeuT [2]; currently a LArTPC called MicroBooNE is under construction, scheduled to begin data collection in 2014. The work presented in this thesis is on behalf of the MicroBooNE collaboration.

The increasing popularity of liquid argon, as well as other liquid noble elements, in neutrino and WIMP detectors has necessitated a deeper understanding of the scintillation light which is produced in these liquids. Known to consist of a prompt

and late component, this light is useful because it encodes the type, energy, and timing of the particle that produced it. However, in a detector only a fraction of the light may be detected due to microscopic quenching. In particular, nitrogen gas can be problematic due to its scintillation quenching properties, abundance in air, and resistance to removal due to its low liquification point of 77 K compared to that of argon, 87 K. Furthermore, previous studies [3] have found evidence for a third component of scintillation light, of time constant intermediate between that of the prompt and late light components. Because theory currently does not account for the presence of a third light component, it is unclear whether this evidence suggests new physics, or an unaddressed experimental systematic.

The neutrino experiment MicroBooNE contains an optical detection system to utilize scintillation light produced in its fiducial volume for event timing and vetos. Indeed, in any timing window there will be not only a potential neutrino event, but also many cosmic ray muon events. The light produced from these muons, in conjunction with the particle track locations, can be used to eliminate cosmic background. In order to facilitate a streamlined installation of the optical detection system happening later this year, a small-scale version has already been implemented in a Vertical Slice Test. Through demonstrating a working system in this test stand, we hope to reduce the time required to achieve a full-scale working system in MicroBooNE itself. We do this through not only characterizing each component in the optical detection system chain, but also through making real physics measurements. More specifically, we measure the rate of quenching as a function of nitrogen impurity concentration, as well as attempt to resolve the number of scintillation light components. Therefore, we can not only demonstrate full operation of the components involved in MicroBooNE's optical detection system, but we can also reach two significant physics results.

1.1 Thesis Outline

This thesis will disseminate the study performed with the MicroBooNE Vertical Slice Test test stand to determine the effect of nitrogen gas impurities in liquid argon on

scintillation light. It also describes preliminary attempts at resolving the number of components in liquid argon scintillation light.

Chapter 2 delves into the background and theory behind the material presented in later chapters. It first describes the history of neutrinos and highlighting the course of events which have led us to our current knowledge of neutrinos today. Second, we highlight the microscopic processes by which liquid argon scintillation light is produced and describe the different mechanisms which produce the prompt and late light. It also describes the phenomena of light quenching by impurities. This is followed by a description of the MicroBooNE experiment, and finally a set of calculations necessary to the nitrogen impurity study.

Chapter 3 presents the Vertical Slice Test which is currently underway. It describes the setup in detail, ranging from the contents of the cryostat to the external electronics used in data collection and processing. We also discuss many of the subsystems required, such as the gas and liquid monitoring lines and nitrogen gas fill line.

Chapter 4 describes the current state of the study to confirm or rule out the existence of a third light component, including data collected, a discussion of analysis methods used, and results.

Chapter 5 contains the description and results of the nitrogen impurity study, and is the core of this thesis. It begins with the data taking procedure and data taken. The analysis methods used are then described, with our analyzed results and interpretation concluding.

Chapter 6 concludes with a summary and discussion of future work in progress to extend these studies.

Three appendices are included which reprint relevant papers and a technical report on which I was an author. They address recent research and development on wavelength shifting coatings used in the detection of liquid argon scintillation light, as well as work done for the Vertical Slice Test during the summer of 2012.

Chapter 2

Background and Theory

2.1 Neutrinos

2.1.1 Postulation and Discovery

Neutrinos have had a most inauspicious beginning. In 1930, Austrian physicist Wolfgang Pauli first suggested their existence as a "desperate remedy" to explain the apparent energy loss and therefore preserve energy conservation in beta decay [4]. He originally named them neutrons, and so they lost their name to the nucleon which now bears its name when it was discovered two years later. Due to the continuous energy distribution of electrons produced in beta decay, the neutrino was widely believed to be massless. Indeed, Pauli attributed the elusivity of the particle to its neutral charge and proposed zero rest mass, postulating that it only interacts through the weak nuclear force. In fact, it wasn't until 1956 that the neutrino's existence was experimentally confirmed, when Clyde Cowan and Frederick Reines of Los Alamos National Laboratory detected antineutrinos produced in a nuclear reactor through inverse beta decay.

2.1.2 Solar Neutrino Problem

Our sun is a constant source of neutrinos: it produces energy through multiple nuclear fusion reactions, which create a certain flavor of neutrino called the electron

neutrino. These particles are also referred to as solar neutrinos due to their origin, and are radiated from the sun isotropically. In fact, because neutrinos are so weakly interacting, only about 1 in 100 billion does not leave the sun. By understanding the sun's nuclear processes, a theoretical calculation of the solar neutrino flux on earth can be obtained.

This calculation was performed, and an experiment was first designed to verify the theory in 1964 by Raymond Davis Jr. and John N. Bahcall. However, their five month experiment yielded only one-third the expected number of detected neutrinos. As the solar model gained precision and accuracy through improved measurements and increased knowledge of the sun, physicists of the time began to question Davis and Bahcall's experimental method. Several other possible explanations arose as well [5]. First, it was possible that neutrinos decayed or otherwise changed into other particles during their journey between the sun and earth. Second, the theory of neutrino interactions may have been inaccurate in concluding that almost all solar neutrinos were radiated from the sun, or the sun's intense magnetic fields may have affected neutrinos through small magnetic moments. To probe these possibilities, other groups joined the solar neutrino search.

These groups, including the Kamiokande collaboration between the United States and Japan and the Sudbury Neutrino Observatory in Canada, found the solution to this solar neutrino problem. By this time, it was known that there were in fact three flavors of neutrinos: the electron, muon, and tau neutrino, named for the corresponding lepton which accompanies them in nuclear reactions (see figure 2-1). They found that the total neutrino flux of all three flavors, combined, was equal to the predicted flux from electron neutrinos produced in the sun. This suggested that neutrinos can change flavor as they traverse the sun. According to theory, this mandates that the particles have nonzero mass, and can oscillate.

2.1.3 Oscillation Parameters and Mass

Many neutrino experiments since have focused on neutrino oscillation and the values of the parameters which dictate the probabilities with which any given flavor will

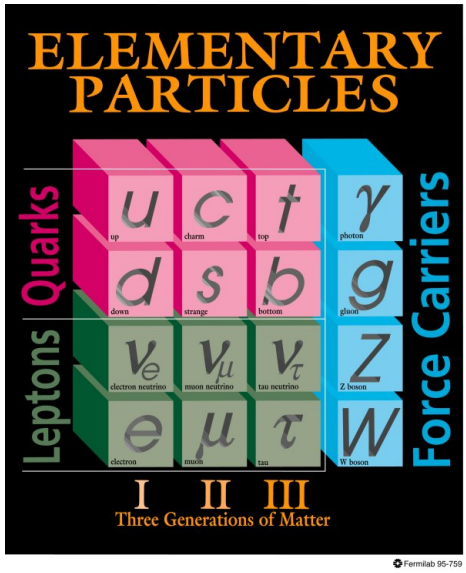

Figure 2-1: The three flavors of neutrinos comprise half of the leptons in the Standard Model of particle physics. Image courtesy of Fermilab. (Higgs boson not included in image.)

be detected as any other given flavor. These parameters include the three neutrino squared mass differences, neutrino energy, and overall oscillation parameters which are constants of nature. Since squared mass differences rather than absolute masses factor into oscillation, physicists are also trying to determine the neutrino mass hierarchy, or the relative ordering of neutrino masses. The overall mass scale is also currently unknown, however it has been limited to the smaller than eV scale [6].

2.2 Scintillation Light in Liquid Argon

Liquid noble elements lend themselves well to particle detection for several reasons. First, as noble elements, they are inert and will not chemically react with other atoms or molecules, creating a stable target volume. Second, they will produce scintillation light and ionization electrons when ionizing particles, such as those produced by neutrino scatters, interact with them. This allows for the reconstruction of particle tracks and dE/dx measurements, as well as for the light collection necessary for additional timing information and vetos.

Argon in particular is a good choice for neutrino detection because its density is

sufficiently large that one can achieve high tonnage in an acceptable volume. It is also much more readily available than the larger noble elements, such as krypton or xenon. Finally, because argon's boiling point is higher than that of nitrogen's, it is produced during the process of liquid nitrogen production, and thus is not too expensive.

When an energetic particle passes through liquid argon, it may ionize or excite an argon atom. This creates the electrons which are drifted via an electric field for track reconstruction. However, the argon atom may combine with a ground state neutral argon atom- as well as an electron if it was ionized- to form an excited argon dimer, or excimer. The excimer will decay back into two ground state argon atoms, releasing the extra energy as a 128 nm photon. The characteristic decay time of this process depends on whether the excimer is in a singlet or triplet state. In particular, the singlet state has a decay time of 6 ± 2 ns, and thus this light is referred to as prompt light. The late light comes from the triplet state excimers, with a characteristic lifetime between 1250 ± 50 ns [3] and 1600 ± 100 ns [7]. Furthermore, the relative ratio of prompt to late light produced depends on the particle dE/dx. Therefore, scintillation light measurements can reveal not only the particle's deposited energy, but its identity as well.

2.2.1 Scintillation Light Quenching

Certain impurities, such as oxygen and nitrogen gas, have been shown to cause quenching of liquid noble element scintillation. More specifically, these impurities can collide with argon excimers and release the extra energy as kinetic energy, rather than through the release of a photon. Not surprisingly, the level of quenching is greater for late light than prompt light, simply because the late light producing excimers have a longer lifetime and therefore a higher probability of collision with an impurity. Therefore, the late light time constant is inversely proportional to the concentration of impurity, however the exact relationship will be measured in chapter 5 and compared to [3].

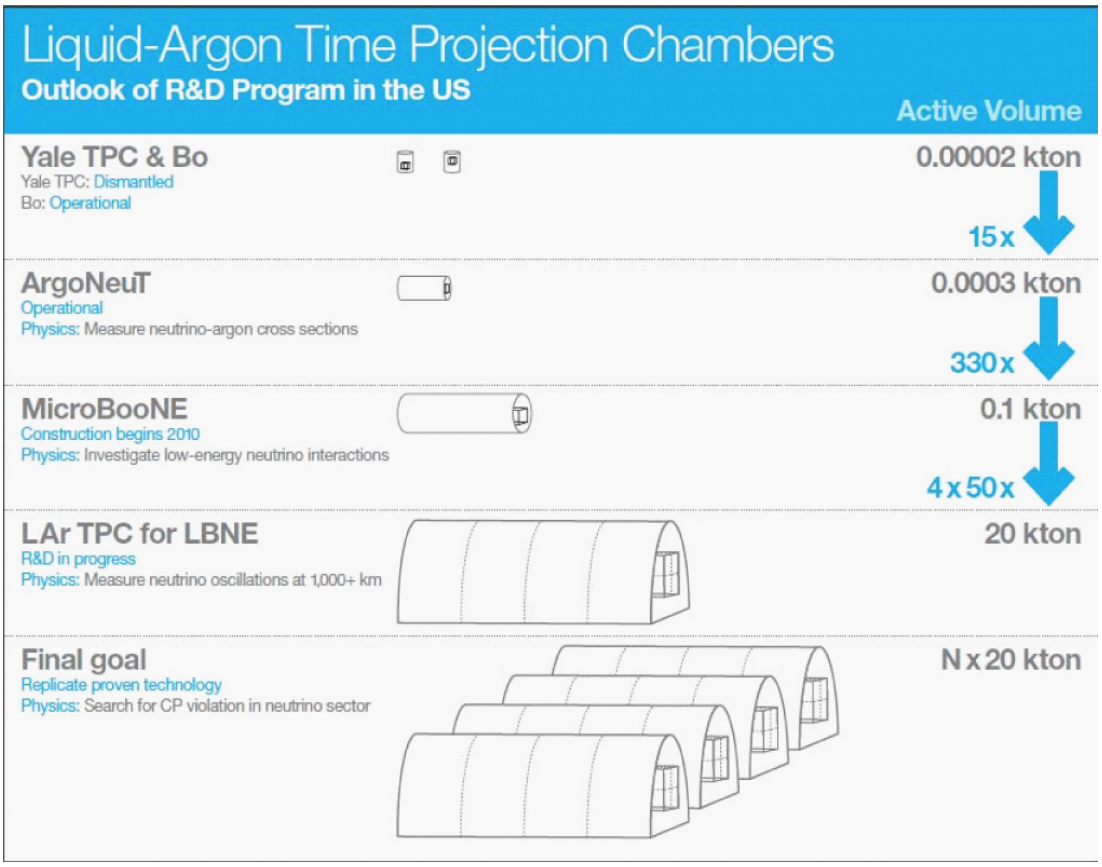

Figure 2-2: MicroBooNE is the next stage in the United States research and development program for liquid argon time projection chambers. Image courtesy of the MicroBooNE collaboration.

2.3 MicroBooNE

MicroBooNE, which stands for the Micro Booster Neutrino Experiment, is a neutrino experiment designed for three main purposes. First, it is meant to further explore and explain the excess of low-energy neutrino events seen by its predecessor, MiniBooNE. Second, it will be used to study the potential existence of a new type of neutrino called a sterile neutrino. Finally, as the largest LArTPC in the United States, it is instrumental in the development of these types of detectors on a large, kiloton scale.

The MicroBooNE detector, like its predecessor MiniBooNE, will be placed on the Booster neutrino beam line at Fermi National Accelerator Laboratory in Batavia, Illinois. It is currently under upgrade, with plans to begin taking data in 2014.

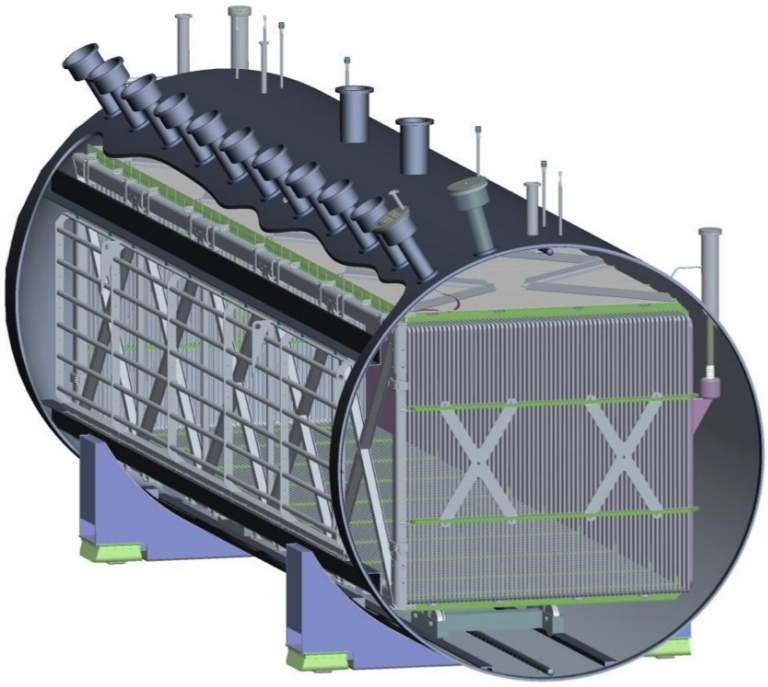

Figure 2-3: A diagram of the MicroBooNE time projection chamber. The field cage consists of the inner rectangular prism, supported by the X-shaped braces. Image courtesy of the MicroBooNE collaboration.

2.3.1 Time Projection Chamber

MicroBooNE consists of a 60-ton fiducial volume of liquid argon as the medium with which neutrinos interact. These interactions produce ionizing particles which, as they pass through the argon, can ionize the atoms and produce a trail of electrons. An electric field placed across the volume then drifts the electrons to one side, where wire planes detect them. This set of wire planes, in addition to the anode and cathode which create the drift field, comprise the time projection chamber of MicroBooNE. This chamber allows for the reconstruction of particle tracks, capable of revealing the particles' energies. A diagram of MicroBooNE's time projection chamber can be seen in figure 2-3.

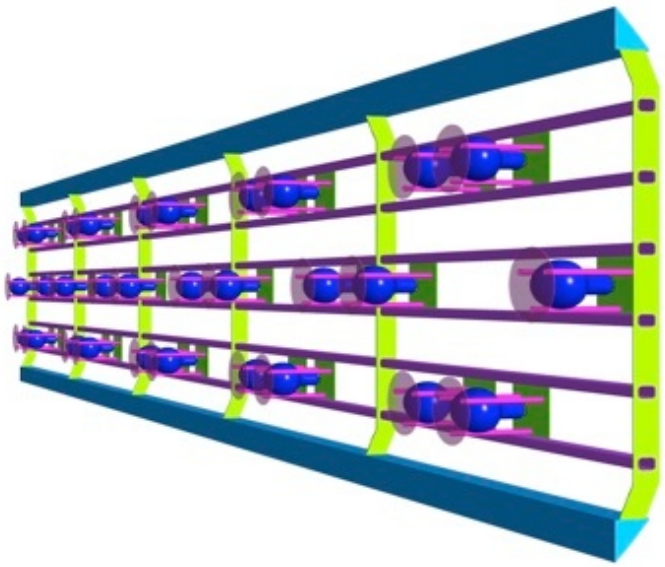

Figure 2-4: A diagram of the MicroBooNE PMT rack, which will be placed behind the field cage. The PMTs are arranged so that they are not hidden behind the X-shaped supports, yet can detect light along the length of the detector. PMTs are in blue and the TPB-coated plates are in semi-transparent purple. Image courtesy of the MicroBooNE collaboration.

2.3.2 Optical Detection System

The liquid argon also produces scintillation light as ionizing particles pass through them, as mentioned in section 2.2, which can then be used to provide additional timing information for particle tracks or as vetos for background events. However, the light produced has a peak wavelength of 128 nm, which lies in the vacuum UV region and cannot pass through the glass of photomultiplier tube (PMT) light detectors. Therefore, the organic chemical tetaphenyl butadiene (TPB) is used to wavelength-shift the light to a 425 nm wavelength, which is in the visible spectrum and can enter PMTs[1]. In MicroBooNE, then, each PMT will reside in a module with a TPB-coated acrylic plate above it. As seen in figure 2-4, a total of thirty modules will be placed along the length of the detector volume so that light information can be correctly matched to particle tracks. This constitutes its optical detection system.

[1]See Appendix A to learn more about TPB and causes of its degradation on the hour-long scale.

2.4 Calculation of Nitrogen Concentration in Argon Liquid

As our scintillation light measurements depend on the concentration of nitrogen gas in the liquid phase of argon rather than in the gas phase, we would like to determine the discrepancy between the two concentrations. Indeed, at fixed volume equilibrium, the concentration of nitrogen in liquid argon does not necessarily equal the concentration of nitrogen in the gaseous argon. We use this calculation to confirm that the nitrogen measurement of the liquid line sample accurately reflects the concentration in the liquid.

The calculation is comprised primarily of Raoult's Law. Our derivation follows that of [8], chapters 8 and 9.

2.4.1 Derivation of Raoult's Law

We assume that both the liquid and vapor phases in our system behave as ideal solutions. By definition, then, each component i has chemical potential μ_i given by:

$$\mu_i = \mu_i^* + RT \ \ln x_i \tag{2.1}$$

where μ_i^* is the chemical potential of the component as a pure substance under the same conditions. R is the ideal gas constant, T is the temperature, and x_i is the molar fraction of component i.

From the definition of fugacity f, we have also:

$$d\mu_i|_T = RT \ d \ \ln f_i|_T \tag{2.2}$$

Now we can differentiate equation 2.1 with constant T, equate it with equation 2.2, and integrate. This gives us a relationship between two different states 1 and 2 in the same phase.

$$\frac{\bar{f}_{i,2}}{\bar{f}_{i,1}} = \frac{x_{i,2}}{x_{i,1}} \tag{2.3}$$

Notice that the bar is used to denote the fact that component i is in a solution.

By taking one of these states to be a pure composition ($x_{i,1} = 1$ and $\bar{f}_{i,1} = f_{i,1}$), we then have a relation for an ideal liquid or gas solution:

$$\bar{f}_i^L = x_i f_{i,P}^L \tag{2.4}$$

$$\bar{f}_i^V = y_i f_{i,P}^V \tag{2.5}$$

From here on, we use x_i to describe the liquid mole fraction, and y_i to describe the vapor mole fraction.

Now, thinking about the vapor-liquid equilibrium as a whole, we know that at equilibrium, $dG_{T,P} = 0$. We also have in general:

$$dG = V\ dP - S\ dT + \sum_i \mu_i\ dN_i \tag{2.6}$$

for volume V, pressure P, entropy S, and number of moles N.

In our system, we assume that both the liquid and gas phase have the same pressure and temperature. Furthermore, since there are no chemical reactions occuring, we can assume that an increase in mole number of the gas necessarily means a decrease in mole number of the liquid by the same magnitude. Thus, for phases α and β, we have that:

$$\sum_i (\mu_i^\alpha - \mu_i^\beta)\ dN_i^\alpha = 0 \tag{2.7}$$

Now, since the differentials for each component are independent of each other and not all zero, for this relation to hold we require that $\mu_i^\alpha = \mu_i^\beta$. Given the relationship between μ and f, we can also say that $\bar{f}_i^V = \bar{f}_i^L$. Now we use equations 2.4 and 2.5 to find:

$$y_i f_{i,P}^V = x_i f_{i,P}^L \tag{2.8}$$

Finally, for an ideal fluid, $f_{i,P}^V = P$ and $f_{i,P}^L = p_i^{sat}$- that is, fugacity equals pressure for an ideal gas, and for an ideal liquid it can be approximated by the saturation pressure.

Thus, we find that for component i in the equilibrium, with liquid mole fraction x_i, vapor mole fraction y_i, system pressure P, and saturation pressure p_i^{sat}, we have:

$$y_i P = x_i p_i^{sat} \tag{2.9}$$

This is known as Raoult's Law.

2.4.2 Application to Experimental System

Let argon be component 1, and nitrogen be component 2. Then we have:

$$y_1 P = x_1 p_1^{sat} \tag{2.10}$$

$$y_2 P = x_2 p_2^{sat} \tag{2.11}$$

$$x_1 + x_2 = 1 \tag{2.12}$$

$$y_1 + y_2 = 1 \tag{2.13}$$

The second two equations come from the fact that within each phase, there exist only the two components under consideration.

The pressure of our system is constantly monitored, and so can be determined without difficulty. The parameters p_1^{sat} and p_2^{sat} can be determined by first determining the temperature of the system. Because the system is primarily comprised of liquid argon, and both liquid and vapor phases are present within Bo, we must lie on the liquid-vapor curve of the argon phase diagram [9]. This yields the system temperature, given its pressure. Notice also that P then equals p_1^{sat}. We can then determine p_2^{sat} by looking up in [9] the pressure corresponding to the system pressure

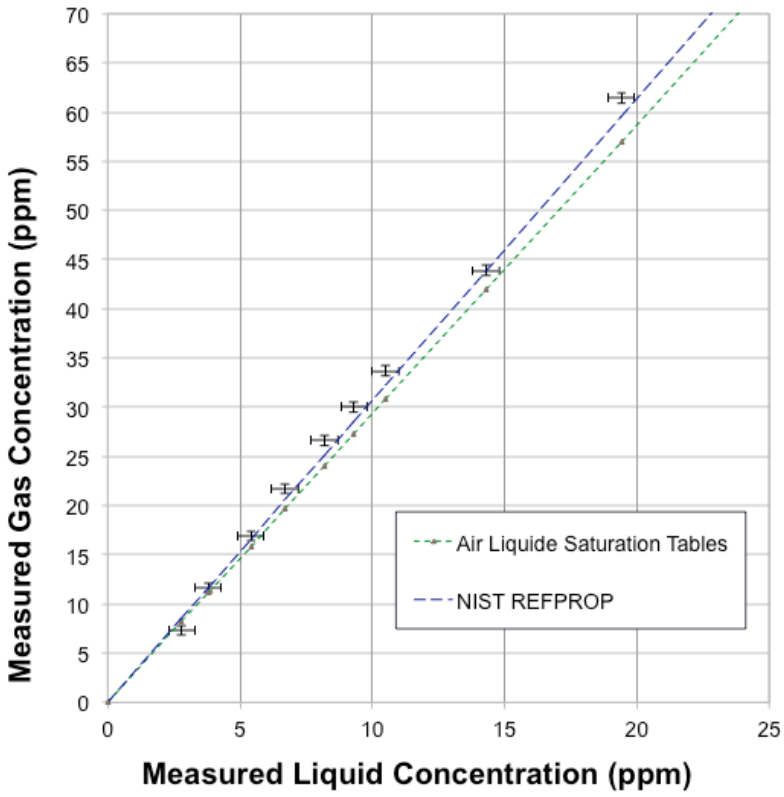

Figure 2-5: Measured nitrogen concentration in liquid argon versus in gaseous argon, along with predictions from our model and NIST REFPROP software. Plot created by Ben Jones.

in the liquid-vapor curve for nitrogen.

Knowing these parameters, we can determine the relationship between the concentration of nitrogen in the gas and in the liquid. This is shown in figure 2-5, along with predictions from the REFPROP software developed by NIST. Our measured values of gas and liquid concentration are in agreement with our calculations.

Thus we confirm that the measured nitrogen concentration from sampling the liquid line is indeed an accurate reflection of the actual nitrogen concentration in the liquid. This is very reasonable, considering that the net flux of nitrogen into the pipeline must be zero.

Chapter 3

Vertical Slice Test

The optical detection system for liquid argon scintillation is a relatively new development. To test it thoroughly before installation, a Vertical Slice Test is currently under operation. The main goal of this test is to demonstrate understanding and operationability of the optical detection system, from light creation to PMT module, to electronics and even data analysis. As part of this task, the test stand is used to reproduce physics results and make new measurements. In particular, in the studies discussed here, the MicroBooNE Vertical Slice Test will be used to measure scintillation light quenching due to nitrogen gas impurities in liquid argon, as well as investigate the potential existence of a third component of scintillation light.

3.1 Experimental Setup

The Vertical Slice Test apparatus is located in the Proton Assembly Building at Fermi National Accelerator Laboratory and centers around a 220 liter cryostat. The cryostat, named Bo, is equipped with an optical detection system and nitrogen injection system. Figures 3-1 and 3-2 contain schematics of these systems.

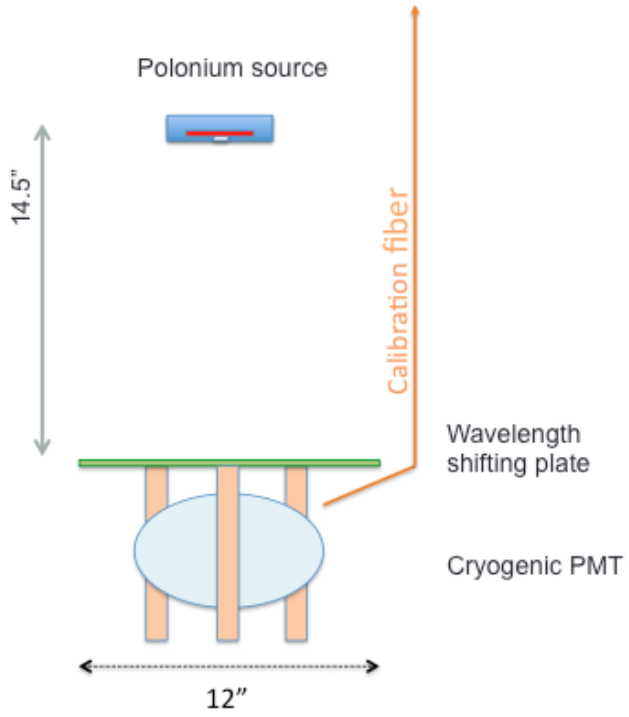

Figure 3-1: Schematic of the optical detection system for the experimental apparatus, including alpha source, calibration fiber for LED, and PMT module. Image created by Ben Jones.

3.1.1 Optical Detection System

The optical detection system in Bo begins with one of the PMT modules which will be installed in MicroBooNE. In these studies, three sources supply light to the PMT for detection. First, a visible LED shone through an optical fiber directed at the PMT provides low-number photoelectron peaks for characterization of the PMT itself. Second, cosmic ray muons are used as a muon source, and third, a polonium sample within the cryostat provides alpha particles of energy 5.3 MeV. Both of these sources create scintillation light, however with differing prompt-to-late light ratios.

Signals from the PMT are sent to an oscilloscope for data acquisition. For data analysis, the oscilloscope saves waveforms to file, where they are processed offline in the ROOT data analysis framework or MATLAB.

During an argon fill, Bo is pumped to a vacuum, then filled with high purity liquid argon to some fixed level. The remaining volume is then argon vapor. The

pressure within Bo is maintained through a nitrogen cooled condenser, which cools argon vapor to the liquid state.

3.1.2 Nitrogen Injection System

The nitrogen injection system consists predominately of two parts: the gas fill line, and the concentration monitoring system. For the fill line, injections are made via a 300 cc gas canister connected to a tank of pure nitrogen gas. The gas canister is first filled with nitrogen to a pressure up to 40 psi, after which the tank is sealed off so that the contents of the canister can be released into the cryostat. A calculation of how each injection affects the ppm concentration of nitrogen is discussed in section 2.4. A vacuum system allows for pumping down of the injection line between injections to keep it clean of argon.

The concentration monitoring system contains a gas phase nitrogen monitor, which measures the concentration of nitrogen gas to a precision of 0.1 ppm. It can sample from either the gas or liquid contents of the cryostat; if it is sampling from the liquid line, the liquid will be in the gas phase by the time it reaches the nitrogen monitor. This system is used in conjunction with our calculations to confirm both the reliability of the monitor and the validity of our predictions, so that we can rely on theory when studying nitrogen concentrations beyond the limit of the nitrogen monitor.

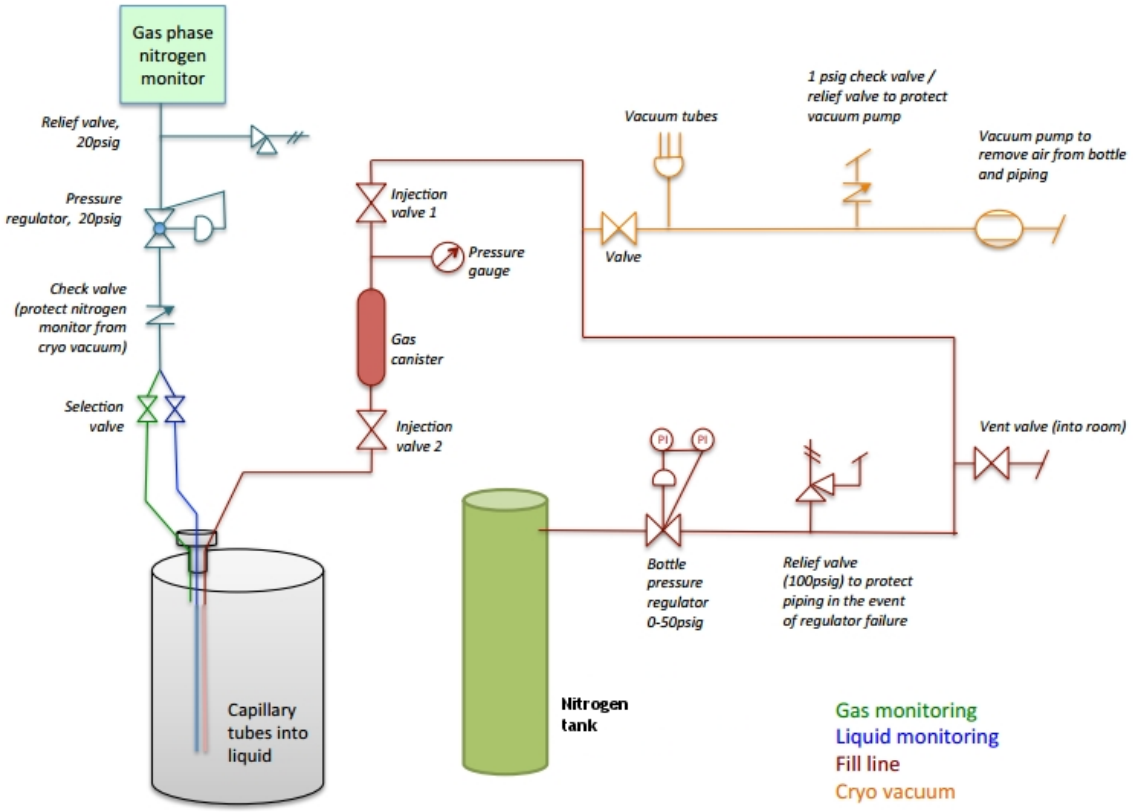

Figure 3-2: Schematic of the nitrogen injection system for the experimental apparatus. Image created by Ben Jones.

Chapter 4

Scintillation Light Components Study

This study regards the possible existence of a third component of liquid argon scintillation light. Theory currently only predicts the presence of two components: prompt light, of time constant 6 ns, and late light, of time constant between 1250 and 1600 ns. However, the WArP collaboration has reported evidence of intermediate light with time constant approximately 40 ns [3]. Therefore, we investigated the number of scintillation light components through the Vertical Slice Test setup, which differs greatly in design from the WArP collaboration setup, in an attempt to determine whether this evidence may have arisen from systematics.

More specifically, the WArP collaboration experimental setup consisted of an 0.7 liter liquid argon cell, which is significantly smaller than our cryostat. Correspondingly, they used a smaller PMT and coated the entire internal volume with TPB to collect as much light as possible. Finally, their light source consisted of a gamma source external to the cell which induced Compton interactions inside, producing electrons which created the scintillation under study [3]. In comparison, we utilized muons and alpha particles. These differences make our measurements very interesting for comparison.

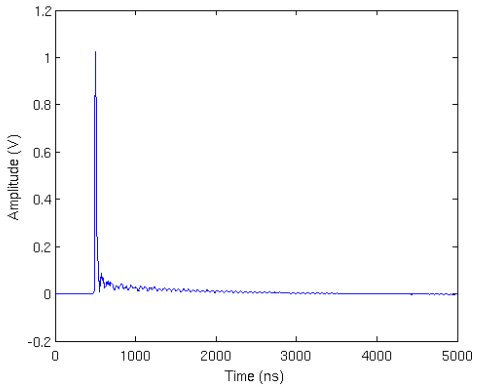

(a) An averaging scintillation response due to cosmic ray muons.

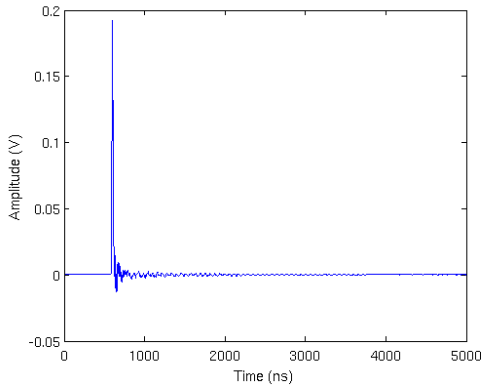

(b) An average calibration pulse. Note the different voltage scales compared to the cosmic waveforms.

Figure 4-1: For scintillation responses and calibration pulses, acceptable waveforms were averaged to reduce noise.

4.1 Procedure

We collected PMT waveforms via the oscilloscope over a total of 5 μs, with a rate of 1 gigasample per second. Since it is unlikely that the number of light components depends on particle type, we studied scintillation light produced by cosmic ray muons rather than alpha particles. A total of approximately 10,000 waveforms were saved. This data set was taken with high purity liquid argon to preserve the light profile as much as possible.

We also collected a similar sized set of calibration data, via the visible LED whose intensity was set to generate single PE pulses in the PMT. This allowed us to account for any effects the PMT pulse shape may have had on the overall light profile.

4.2 Analysis

Our first step in the analysis was to filter out waveforms which could not be used. This included waveforms that saturated the oscilloscope and therefore exhibited cutoffs, waveforms that were so large that they entered the PMT nonlinearity region, and waveforms with multiple large peaks in the window, such as those from multiple events.

The filtered waveforms were then averaged to reduce noise and obtain a single waveform (figure 4-1(a)). A similar procedure was used to obtain an average single photoelectron pulse; the calibration waveforms were filtered to eliminate any that had more than one photoelectron or more than one pulse, and the remaining pulses were averaged to reduce noise (figure 4-1(b)).

At this point, there were two methods which could be used to analyze the number of components in the average cosmic waveform: a Fourier transform deconvolution method, or a fit to a convolved simulated pulse. We describe each in detail.

4.2.1 Deconvolution Method

The preliminary deconvolution method was used to obtain an estimate for the scintillation light time constants and the relative ratios of prompt and late light. Because this method has been further developed and results from this method will be reported at a later date, its exact details will not be disclosed here. However, a brief description follows.

It is very similar to the analysis used in [3], and consists of performing a Fourier transform on the single photoelectron calibration pulse to obtain a deconvolution kernel. This kernel then divides the transform of each average waveform, after which we apply lowpass filtering and a Weiner filter[1]. Finally, taking the inverse Fourier transform of the result yields the desired underlying time profile of scintillation light. A fit to the sum of two or three exponentials via the ROOT framework extracts the necessary fit parameters.

As seen in figure 4-1(a), there were reflections on our pulse which created ringing of frequency approximately 17 MHz. The cause of this has been narrowed to either the PMT signal/high voltage splitter or the cable feedthrough for the cryostat, however the ringing has not been removed yet. For this reason, it was particularly important that we use a Fourier analysis to extract the light profile, rather than attempt to perform a fit to a sum of exponentials directly to the average waveform.

[1]Many thanks to Warren Schapert for his advice on signal processing techniques.

4.2.2 Convolution Fit Method

In this method, an estimate for the scintillation light time constants and the relative ratios of prompt and late light are made, then used to simulate the underlying sum of exponentials that describe the scintillation light produced. This is then convolved with the single photoelectron calibration pulse to produce a simulated average waveform with the underlying exponential seed amplitudes and time constants.

We can obtain a chi squared goodness of fit statistic between our simulated and measured waveforms, which provides a quantitative measure of the accuracy of the simulated waveform's underlying prompt and late light time constants. The statistic is obtained via the equation:

$$\chi^2 = \frac{1}{n}\sum_{i=1}^{n}\frac{(d_i - m_i)^2}{\sigma^2} \tag{4.1}$$

where n is the number of data points, d_i is the ith data point, m_i is the expected value of the ith point according to the model, and σ is the vertical uncertainty on each data point. Then, the local parameter space can be explored to find the lowest chi squared value, to determine the late light time constant for that particular measured waveform. Once this algorithm is repeated for both types of pulses and all nitrogen concentrations, we can determine the relationship between nitrogen impurity level and late light time constant.

Because the deconvolution method is still under development and will be reported on at a later date, in this analysis we use it only to create initial seed parameters for the convolution method.

4.3 Two Exponent Model

We used the following sum of two exponentials as our underlying light profile model:

$$V(t) = A \times \mathrm{e}^{-t/a} + B \times \mathrm{e}^{-t/b} \tag{4.2}$$

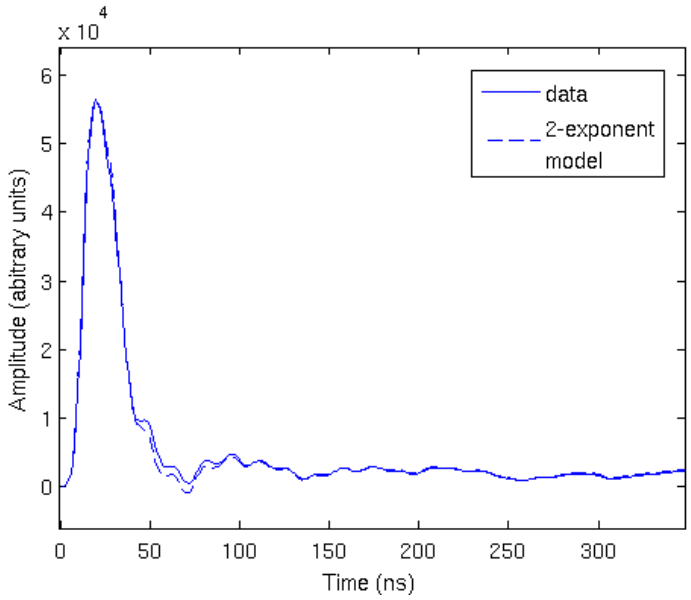

Figure 4-2: As the chi squared statistic converged to a minimum, we saw that our convolved pulse did not converge to the data waveform.

For any set of parameters A, a, B, b, we computed the light profile $V(t)$, convolved it with the single photoelectron calibration pulse, and calculated its chi squared value in relation to the data waveform. To minimize the chi squared, we first floated the amplitude parameters, to reduce a 4-D parameter space to two dimensions. This was done by taking the smallest chi squared value among the different amplitudes for any given pair of time constants. A contour plot was then drawn of the various goodness of fit values, to determine the local minimum. By iterating with increasingly narrow bounds, both time constants were obtained. More specifically, once the parameters were determined within 5%, we achieved our best fit and stopped. The best 2-exponential fit for our average cosmic waveform with no nitrogen contamination is shown in figure 4-2.

Although the chi squared statistic converged to a minimum, its final value equalled approximately 8.387 and it seemed that ultimately, the fit had limited accuracy in the region intermediate to the prompt and late light. In fact, in this region, the convolution was systematically lower than the data. This provided evidence for an intermediate component, as well as reason for exploring a three-exponent fit.

This fit yielded time constants for the prompt and late light of approximately

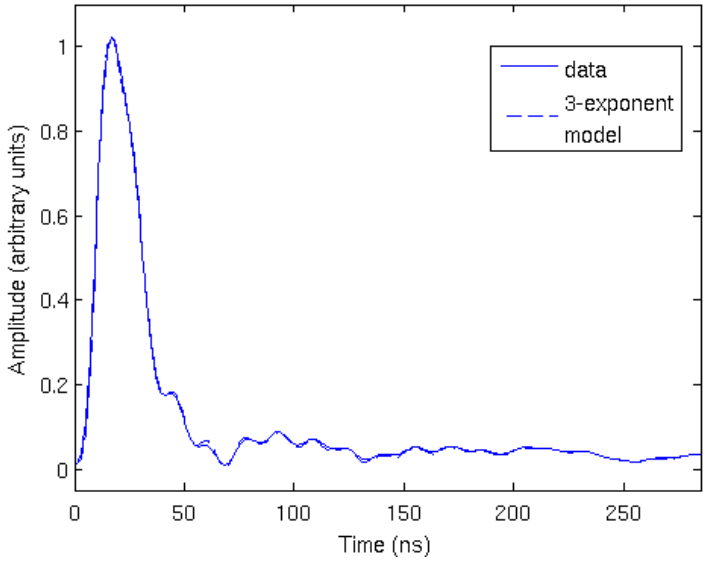

Figure 4-3: Unlike with the two-exponential model, as the chi squared statistic converged to a minimum, we saw that our convolved pulse did converge to the data waveform.

6.151 $\pm$ 0.308 ns and 1229 $\pm$ 61 ns. Despite the poor fit, these values agree with previously published values.

4.4 Three Exponent Model

Similarly, for the 3-exponent fit, we used the following underlying light profile model:

$$V(t) = A \times \mathrm{e}^{-t/a} + B \times \mathrm{e}^{-t/b} + C \times \mathrm{e}^{-t/c} \tag{4.3}$$

The fits were performed in the same way as the two-exponent fits, where the parameters were modified so as to minimize the chi squared statistic, and a similar strategy was implemented to reduce the 6-D parameter space down to three dimensions. The time constants which yielded the lowest chi squared value, then, were used as seeds for the next iteration of fits. We then proceeded to narrow the parameter space until reaching sufficiently precise values. A final best fit for the average cosmic sample with no nitrogen contamination can be found in figure 4-3.

As expected, this third exponential led to a more accurate fit to the data, with a

better chi squared value of 1.863. Therefore, it seemed that there is indeed presence of a third component that must be accounted for in analyses of these light pulses. Crucially, however, the exact cause of this component may not be light-related. More specifically, there may be an element in the system unrelated to scintillation light which creates the slightly different-than-expected light profile.

The fit measured the prompt, intermediate, and late light time constants to be 3.953 ± 0.198 ns, 25.56 ± 1.28 ns, and 1358 ± 68 ns, respectively. This late light time constant, within one standard deviation, just barely overlaps with the corresponding constant measured by WArP, also in the one standard deviation range. However, we would not normally expect close agreement between the two values because the experimental designs differ so greatly.

The prompt and intermediate time constants are smaller than their reported values elsewhere. Crucially, the large difference between our measured intermediate time constant and the previously measured value of 40 ns suggests that the presence of this component may not be from light production processes, but rather from signal processing.

4.5 Analysis

There is a possibility that light with an intermediate time constant is being produced, and several groups have thought about and discussed possible physical phenomena which may explain this [3, 10]. However, its origin may be signal processing-related. For example, there may be nonlinearities in the system which are not reflected in the relationship between pulse height and area. Efforts are currently being made to isolate and assess any potential nonlinearites.

Additionally, the LED light pulse is not a perfect impulse response. Because of this, the single photoelectron calibration pulses may not accurately reflect the pulse shape that should be used for convolution. In fact, the pulse shapes of an LED-induced pulse and a dark rate pulse do differ; this discrepancy may be enough to explain the existence of the intermediate light signal, however further studies are

necessary to investigate this.

It is quite peculiar how with an entirely different experimental and electronics setup, the WArP collaboration also saw evidence of three distinct light components. Since these results have so far been unable to rule out the intermediate light, it will be very interesting to see whether finding and eliminating nonlinearities in the system, or improving the signal processing and data analysis, will be able to solve the issue.

Chapter 5

Nitrogen Quenching Study

As seen in chapter 3, this study involves the injection of nitrogen gas into the liquid component of the argon in Bo. With every injection, the nitrogen will quickly bubble up to the surface, thereby entering the argon vapor. As the system equilibriates, it will begin to re-enter the argon, at which point a measurement can be taken.

5.1 Procedure

Similar to the light components study, we began by collecting PMT waveforms via the oscilloscope over a total of 5 μs, with a rate of 1 gigasample per second. To determine the range of pulse sizes for alpha-dominated and cosmic-dominated regions, we measured cumulative pulse rates as a function of pulse height with and without the alpha source installed. As seen in figure 5-1, this identified the regions where the majority of scintillation light arises from alpha particles, and similarly for cosmics. The pulses were collected following the occurrence of a normal falling trigger, therefore the trigger level was used to set a lower bound on the amplitude of pulses collected.

However, for validity of the analysis methods used, we also required that our PMT behaved linearly in the regions of interest; thus we set an upper bound on pulse amplitudes as well. A scatterplot of peak height versus area (figure 5-2) revealed the regimes of linearity and nonlinearity. Because the transition occurs for very large pulses located far beyond the alpha-dominated region, a cut at the transition sufficed

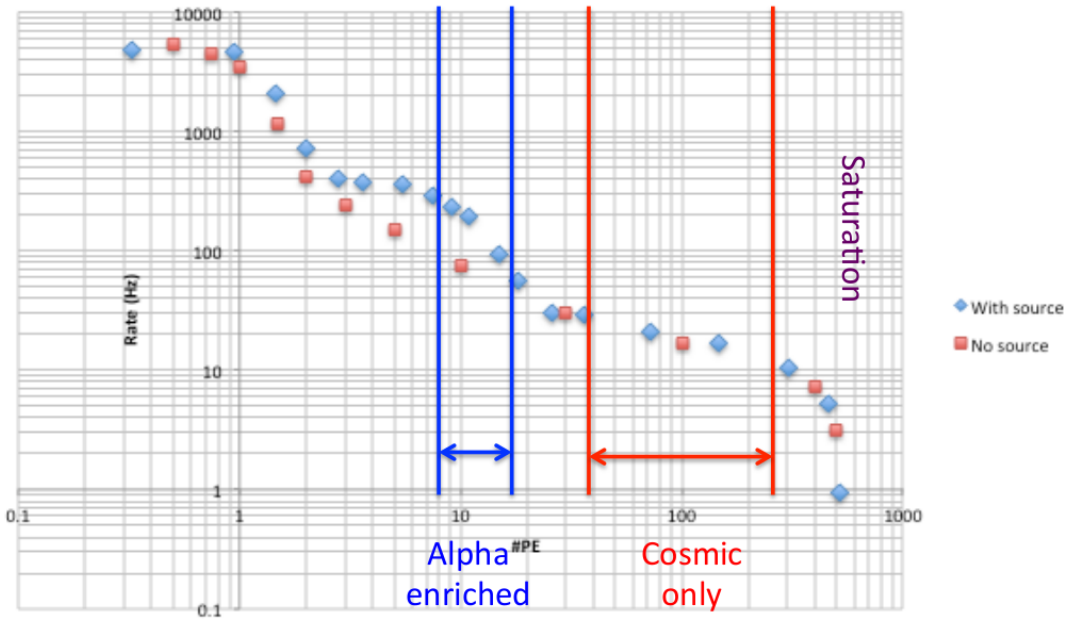

Figure 5-1: The discrepancy in cumulative rates with and without the alpha source installed identified the alpha-rich region. By contrast, the areas with little discrepancy identified the cosmic-rich regions. Image created by Ben Jones.

to eliminate any saturated PMT pulses. Furthermore, to prevent contamination of cosmic pulses in our alpha sample, we made a cut at the upper bound of the alpha enriched range.

In each of these two regimes, we collected waveforms for ten different nitrogen concentrations spanning from 0.4 ppm to approximately 1000 ppm. After each nitrogen injection, the system was allowed to equilibriate for at least 45 minutes, after which the nitrogen concentration measurement varied by at most 0.5 ppm.

More specifically, for each nitrogen concentration we first set the oscilloscope to trigger for pulses in the alpha-dominated region. A total of 10,000 waveforms were collected, then the measurement was repeated for a trigger level corresponding to the cosmic-dominated region. Furthermore, a set of calibration data was taken, via a visible LED set to generate single PE pulses in the PMT.

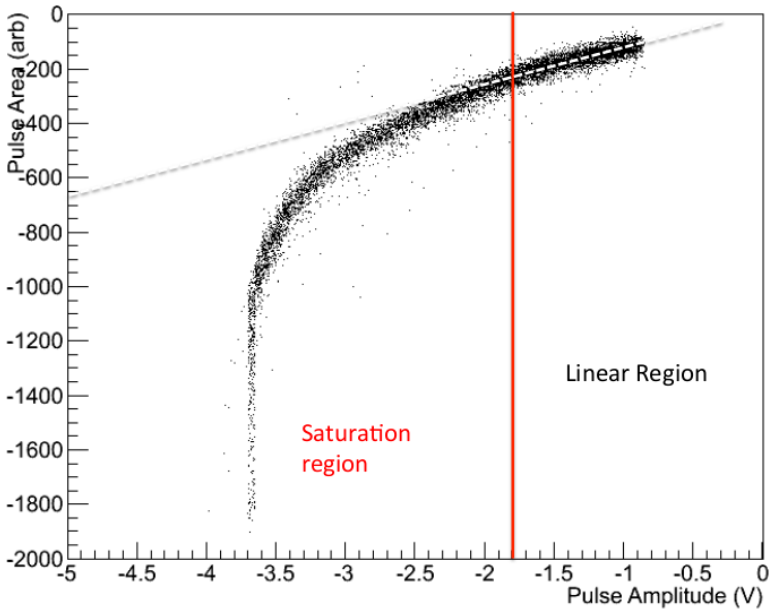

Figure 5-2: A scatterplot of pulse peak height and pulse area revealed the regions where height and area are not linearly related; pulses in this region of nonlinearity were undesireable for our analysis. Plot created by Ben Jones.

5.2 Analysis Methods

The analysis begins in the same way as for the previous study, in which waveforms for each source and nitrogen concentration were first filtered, then averaged. Thus, we achieved one average waveform for each type of pulse- alpha or cosmic- and nitrogen concentration.

The nitrogen concentration in argon liquid was determined through the nitrogen monitor, because the calculations described in section 2.4 have shown that even when sampling from the liquid line, the monitor will give reliable results.

We then implemented the convolution fit method for each of these waveforms, to determine their late light time constants. This was plotted against the nitrogen gas concentration to determine the effect of nitrogen quenching on liquid argon scintillation.

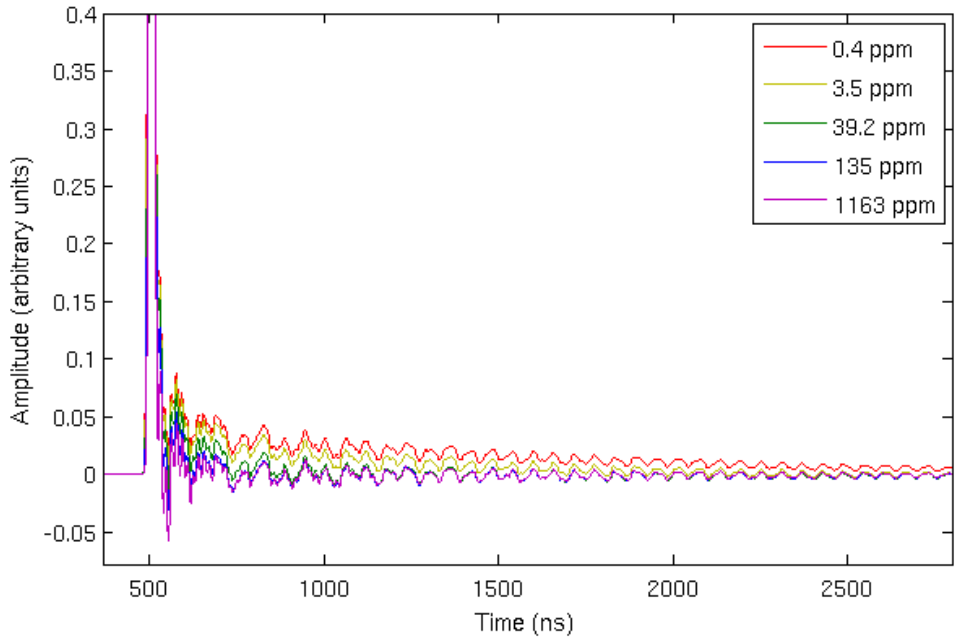

Figure 5-3: Selected averaged waveforms from varying nitrogen concentrations revealed that there is indeed quenching, and that this affects the late light component much more than the prompt light.

5.3 Late Light Quenching Results

There is indeed increasing late light quenching with increasing nitrogen concentration (figure 5-3). By plotting average waveforms from selected concentrations which have been normalized for peak amplitude, we saw that for larger levels of nitrogen contaminant, far less late light was detected.

Figure 5-4 shows the amount of quenching, expressed as the fractional change in late light time constant, for our cosmic-dominated data sets. The plot obtained by the WArP collaboration [3] is also shown for comparison. Unfortunately, because there is a smaller late light to prompt light ratio for scintillation light due to alpha particles, only the first two nitrogen concentrations yielded waveforms from which late light time constants could be extracted. However, for these two data points, there is great agreement with the data from cosmics. Therefore, the small alpha data set is likely not a concern.

For the cosmic waveforms and nitrogen concentrations above 100 ppm, the level

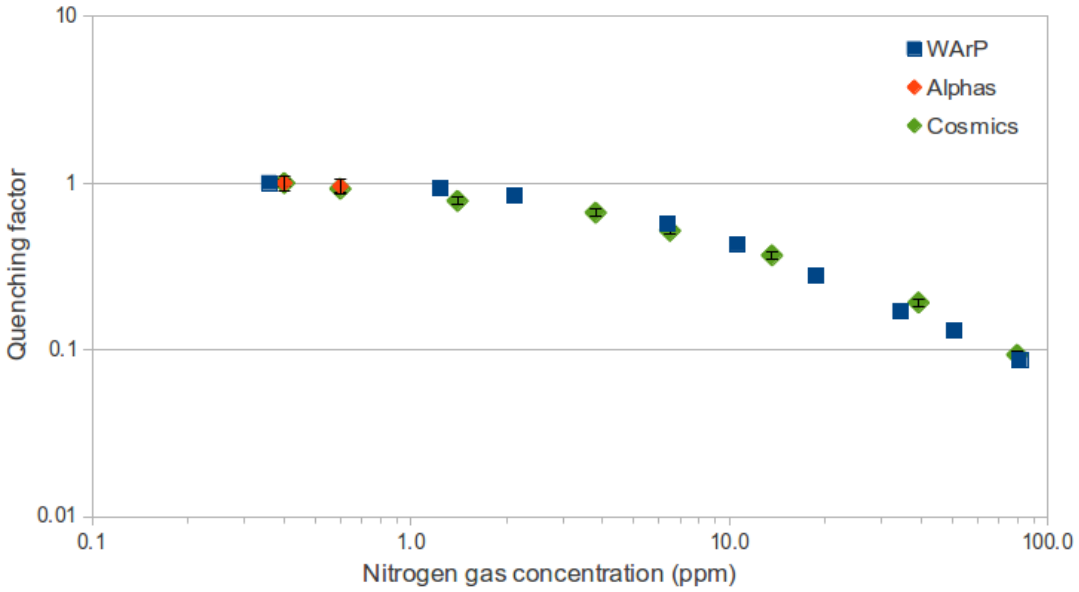

Figure 5-4: Late light quenching for both alpha and cosmic data sets, plotted with WArP data. The data sets are in agreement with each other.

of late light quenching was so great that the late light time constant could not be extracted. However, we may be able to obtain these time constants after further development of our analysis techniques. This concentration seems to be the upper limit of impurity for the WArP collaboration as well.

We have successfully measured the quenching of liquid argon late scintillation light from nitrogen gas impurities. There does not seem to be a simple equation which represents the relationship between these two quantities. However, we conclude that our results are within error of previous measurements.

Chapter 6

Conclusion

The MicroBooNE optical detection system has been characterized and tested thoroughly. This thesis focused on its use for the examination of number of scintillation light components, as well as for the measurement of scintillation light quenching as a function of nitrogen gas impurity. These tests identify three main areas for further development. First, the source of 17 MHz ringing on the PMT waveform should be identified and eliminated to the greatest extent possible. It is immediately clear that these oscillations severly impact our ability to measure the late light time constant; it also masks the region in which a third component of light would dominate. These oscillations also seem to adversely affect our ability to apply the convolution analysis method to waveforms from scintillation due to alpha particles.

Second, the LED single photoelectron pulse should be replaced with a dark rate pulse so that the calibration waveform more closely resembles the PMT response from an impulse. However, in order to maintain the same level of consistency, the entire data set should be retaken. This way, any fluctuations over time in the PMT pulse shape itself will be accounted for through calibration pulses taken right after each data set. This should make the convolution method more reliable.

Finally, the ongoing improvements to the Fourier deconvolution method and examination of nonlinearities in the system may yield useful results regarding the number of light components. More specifically, it may be the case that the intermediate light component comes from an artifact introduced through the complex signal processing.

Although there are several improvements that can be made, from the successes of these studies we see that the current implementation of the optical detection system is very promising for triggers and vetos in the detector. Furthermore, by creating a working prototype outside of the detector, we have been able to isolate several design flaws and remedy them before installation of the system in MicroBooNE. This will ultimately expedite MicroBooNE's construction, and is invaluable development for the future of large scale liquid argon time projection chambers.

MicroBooNE is expected to complete collecting its first full data set in 2017. This data will resolve many of the discrepancies between previous neutrino experiments, including the low-energy excess of MiniBooNE. The new information will also allow us to catch a glimpse of new properties of the neutrino, including whether there are new types of neutrinos in existence known as sterile neutrinos [11]. These particles do not even interact via the weak force, and thus interact only through gravity, by far the weakest of the fundamental forces. This makes them even more difficult to detect than the currently-known neutrinos; however, they may oscillate with the currently-known three flavors of neutrinos, which offers a possible window for detection. The next few years will certainly be an interesting time for MicroBooNE, and for the whole of neutrino physics as well.

Appendix A

Environmental Effects on TPB

This appendix consists of a paper describing an experiment performed to identify and quantify the long term degradation of wavelength-shifting chemical tetraphenyl butadiene (TPB). This chemical is particularly useful in liquid argon time projection chambers, and so it is of interest to determine the storage conditions that will most prolong its usability.

This paper has been published in JINST. My contributions include performing the "Basic Lighting Conditions" study, as well as searching for and analyzing UV-blocking materials as a preventative measure for TPB degradation.

PUBLISHED BY IOP PUBLISHING FOR SISSA MEDIALAB

RECEIVED: *April 25, 2012*
ACCEPTED: *June 17, 2012*
PUBLISHED: *July 4, 2012*

Environmental effects on TPB wavelength-shifting coatings

C.S. Chiu, C. Ignarra,[1] L. Bugel, H. Chen, J.M. Conrad, B.J.P. Jones, T. Katori and I. Moult

Massachusetts Institute of Technology,
77 Massachusetts Avenue, Cambridge MA 02139, U.S.A.

E-mail: cschiu@mit.edu

ABSTRACT: The scintillation detection systems of liquid argon time projection chambers (LArTPCs) require wavelength shifters to detect the 128 nm scintillation light produced in liquid argon. Tetraphenyl butadiene (TPB) is a fluorescent material that can shift this light to a wavelength of 425 nm, lending itself well to use in these detectors. We can coat the glass of photomultiplier tubes (PMTs) with TPB or place TPB-coated plates in front of the PMTs. In this paper, we investigate the degradation of a solution-based, embedded TPB coating in a laboratory or factory environment to assess the viability of long-term TPB film storage prior to its initial installation in an LArTPC. We present evidence for severe degradation of this type of coating due to common fluorescent lights and ambient sunlight in laboratories, with potential losses at the 40% level in the first day and eventual losses at the 80% level after a month of exposure. We determine the degradation is due to wavelengths in the UV spectrum, and we demonstrate mitigating methods for retrofitting lab and factory environments.

KEYWORDS: Scintillators, scintillation and light emission processes (solid, gas and liquid scintillators); Noble-liquid detectors (scintillation, ionization two-phase); Time projection chambers

[1]Corresponding author.

doi:10.1088/1748-0221/7/07/P07007

2012 JINST 7 P07007

Contents

2012 JINST 7 P07007

1 Introduction

Liquid argon time projection chambers (LArTPCs) are appealing due to their excellent energy resolution and particle reconstruction capabilities. In these detectors, we apply a voltage across a volume of liquid argon (LAr). A charged particle traveling through the argon will ionize the atoms along its path, producing a track of ionization electrons that then drift towards the wire planes of the TPC due to the applied electric field. A typical design [1–3] has three wire planes for detection: two induction planes, which measure the current induced in the wires by the approach of the ionization electrons, and one collection plane. The dE/dx of the charged particles can be reconstructed from this information, as can their 3D tracks. This allows for excellent particle identification of tracks and showers, with millimeter-level spatial resolution [1].

This technology is relatively new and its development is rapidly progressing. Previous LArTPCs and successful training grounds for technology in particle physics include ICARUS [2] and ArgoNeuT [3]. Upcoming experiments include MicroBooNE, which is scheduled to begin taking data in 2014. These are all precursors to the ultra-large detectors proposed for future long-baseline experiments, such as the Long-Baseline Neutrino Experiment (LBNE) [4], and will help us to determine the viability of LArTPCs as an option for this large-scale neutrino program.

Another feature of this technology is that charged particles passing through LAr produce scintillation light which can be detected to provide useful additional information. It is advantageous for the experiment to use this light in trigger and veto systems: a TPC takes order 1 ms to detect an ionization electron, compared to order 6 ns to detect scintillation light. Also the light can provide the interaction time T_0 for track reconstruction. This is especially important for non-beam physics because, unlike with beam events, we do not have the spill timing to obtain a sufficiently accurate T_0 [5]. Unfortunately, LAr scintillation light is produced at 128 nm and, therefore, must be shifted to visible wavelengths for detection. This is typically performed using the wavelength shifter TPB.

As detector size grows, construction and installation will inevitably require larger spaces and production-based environments. This paper explores how aspects of a typical detector assembly environment can affect the TPB used in LArTPC light collection systems and suggests practical methods to mitigate these effects. We begin by describing a robust coating method for applying TPB that can survive handling in a large assembly area without imposing excessive costs. Next we focus on the effects of exposure to ambient laboratory light on this TPB coating. We then turn to other light spectra and explore their effects on TPB degradation. We end with a set of practical recommendations for constructing and handling light collection systems for LArTPCs.

2 Light detection in liquid argon

Scintillation light is produced from the decay of argon excimers, which can be created by the passage of a charged particle. The decay proceeds via either a fast or a slow path and results in two individual argon atoms and a 128 nm photon. The fast path has a time constant of 6 ± 2 ns, representing a decay from a singlet state argon excimer, and the slow path has a time constant of 1600 ± 100 ns, representing decay from the triplet state. Experimental values for both minimum ionizing particles (MIPs) and heavily ionizing particles fall within these errors [6, 7]. The percentage of total scintillation that arises from the fast path increases with increasing ionization density. Using a MIP as an example, the fast component accounts for about 23% of the scintillation light. For a detailed review of light production in argon see references [6, 7].

The scintillation light, at 128 nm, lies in the vacuum UV range and thus cannot pass through many materials, including air and glass. Its wavelength must be shifted to allow for detection. TPB lends itself well to this task given that it absorbs UV light and re-emits it in the visible spectrum at a peak wavelength of 425 nm. We can implement light conversion through applying a TPB film to the glass of the PMTs [2], or to separate plates [5] or lightguides [8] which can then be placed in front of the PMTs. This allows any light reaching the PMTs to be shifted to a wavelength that can pass through the PMTs' glass envelopes.

3 TPB-coated plates and test stand used in this study

3.1 Application of TPB to acrylic plates

The efficiency, in terms of photons out per photon in, for re-emission of light absorbed at 128 nm has been determined to be 120% for a film of pure TPB made through vacuum evaporation [9]. This follows energy conservation because the re-emitted photons have a lower average energy than the

2012 JINST 7 P07007

Figure 1. A typical plate used for our studies. The acrylic plate is clear, and the TPB coating has a milky appearance. Two holes were drilled into the plate for attachment to our testing apparatus (figure 2).

incident light. However, we have observed that evaporative coating on acrylic handled in a lab environment is not resilient [5], presumably due to absorption of water by the TPB and/or acrylic [10]. Construction of a large light collection system would be extremely expensive if the acrylic must be maintained free of water. Therefore, we have looked to other, more resilient coatings.

We are analyzing a number of different coating mixtures, and they will be reported elsewhere. For this study, we used a coating of 50% TPB and 50% polystyrene (PS) by mass, which will be used in the MicroBooNE experiment. This has been measured to have about 50% of the efficiency of the evaporative coating [5]. We found that using mixtures such as these makes the plates more durable, likely because the TPB is partially embedded in PS from the solution. Furthermore, this type of film will be much more cost-effective for large systems.

To adhere the TPB to each plate, we created a TPB solution consisting of a 1:1:43 ratio by mass of PS to TPB to toluene. Each acrylic plate required three coatings of the TPB solution (figure 1). For this study, each plate measured approximately 4 inches square; however, larger plates are planned for MicroBooNE. For each coating, we applied about 2.5 to 3 mL of solution onto the test plate and distributed it evenly with a brush by hand. The solution temporarily dissolved any previous coatings from the plate, leaving a more concentrated solution of TPB+PS in toluene. The toluene then evaporated, leaving behind a thin film of TPB embedded in PS. Because they were applied by hand, there were inevitable inhomogeneities in the coatings. Consequently, we tested the performance of two locations on each plate when monitoring the possible degradation of TPB in a laboratory environment.

3.2 Testing plate performance

The following tests used the apparatus shown in figure 2 to measure plate response. It comprised a 50 cm x 8 cm x 96 cm dark box with a PMT attached to one side. On the opposite side we placed a StellarNet Inc. SL3 deuterium lamp filtered to emit wavelengths at 214 ± 5 nm. The lid was fitted with a rod which extended into the box, and to which we could attach an acrylic plate. To test different locations on the plate, it could be lifted independently from the lid to a consistent height. Plate performance was quantified using the number of PMT pulses obtained above a threshold of 30 mV in a designated time interval. The deuterium lamp output was collimated so that typical measurements ranged from about 12,000 counts/sec for a degraded plate to 70,000 for a newly

2012 JINST 7 P07007

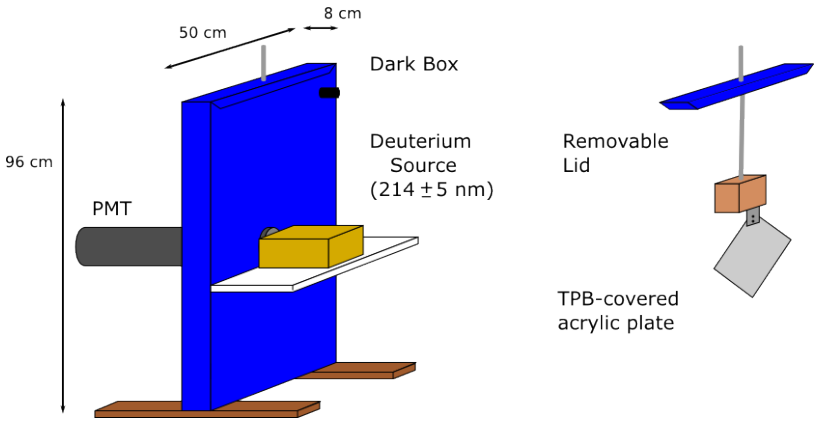

Figure 2. The plate performance test stand consisted of a dark box with a PMT and deuterium source. The plate could be lifted independently of the lid to test different locations on the plate.

made plate. The dark rate for pulses over 30 mV equaled 260 ± 5 counts, and thus could be regarded as negligible.

4 Basic lighting conditions

4.1 Setup

We began by examining solution-based TPB film performance after extended exposure to four common laboratory lighting conditions. After applying the TPB film and recording their initial performance levels, we placed groups of three plates in one of four conditions. Three of these groups were placed into lab humidity, but each was exposed to a different kind of light: common fluorescent light, amber light, or no light. The fourth condition kept plates in the dark, but also contained reduced humidity levels to examine whether humidity was a concern for plate degradation in the long run.

The plates were kept in their respective environments for about a month, and their performances were initially monitored every one or two days. TPB plate performance was assessed by averaging the PMT count rate from the testing apparatus with the plate in place, sampled for two different locations on the plate. However, we have noticed downward drifts in PMT sensitivity by about 8% in five minutes, as well as in the deuterium source output over several hours. Therefore, we let the PMT stabilize for at least five minutes and the source for at least three hours before use. We accounted for any remaining fluctuations by introducing a reference plate: a TPB-coated plate that has already reached an approximately steady state degradation and, therefore, would not change in performance over the course of our study. This reference plate was also kept in the dark to ensure its stability. By measuring the performance of the reference plate before and after each testing session, we could normalize each plate relative to the reference and track this normalized performance over time.

2012 JINST 7 P07007

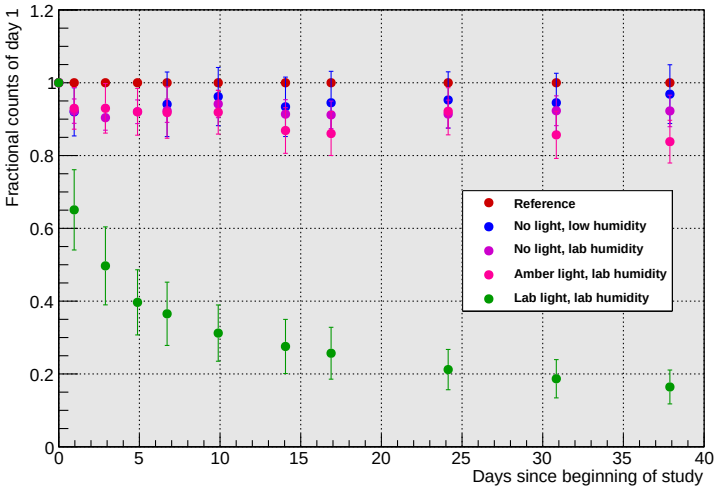

Figure 3. Degradation of TPB films due to various lighting conditions, as fractions of their performance on the day that they were created. Data has been normalized to a reference plate.

4.2 Results

The average count rates per plate and per storage condition were computed for each day and normalized to the reference plate averages. Plate performance, expressed as a percentage of Day 1 performance, is plotted for each plate condition in figure 3. Sources of error included fluctuations in the testing apparatus and plate inhomogeneity.

Our results are quite striking; within one day, we observed roughly 35% degradation of embedded TPB due to common laboratory lighting conditions. In comparison, plates exposed to amber light or no light experienced less than 10% degradation. We believe the initial drop in the dark- and amber-stored plates was due to the light exposure from creation to initial testing. Furthermore, after five weeks these samples still exhibited similar performance levels, suggesting that degradation over these timescales due to amber light, no light, or lab humidity is not of major concern. Five weeks of exposure to ambient lab light, however, was quite detrimental: our plates demonstrated less than 20% of their original wavelength-shifting ability. Thus we observe the harm done to our TPB films due to unfiltered light, with detrimental effects on a timescale of less than a day.

5 Exposure to restricted light spectra

5.1 Setup

We introduced five ranges of light wavelengths to test solution-based TPB-coated plates. Each condition exposed the plates to a different spectrum of light by means of a full spectrum fluorescent light shone through various light filters. Each filter was centered around either amber, blue, green, cyan, or red, although each filter also let through some light at other wavelengths. All of the spectra under consideration are displayed in figure 4.

2012 JINST 7 P07007

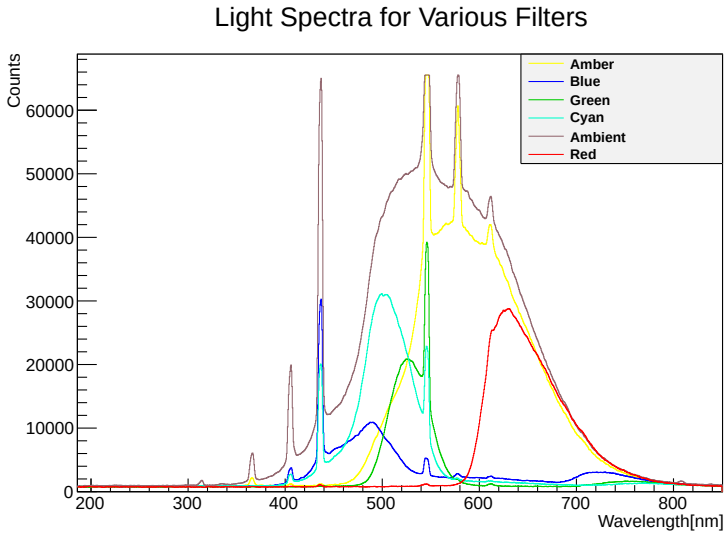

Figure 4. Spectra of full spectrum fluorescent light after it passes through one of the colored filters. The peaks arise from emission lines in the lamp.

We tested the plates every three to four days for approximately a month using the method described in section 4.1. After sixteen days, we increased the intensity of light to which all plates were exposed. This was done to better distinguish whether TPB films were degrading slowly or not at all. We did this by halving the distance between plates and the fluorescent light source.

5.2 Results

Figure 5 plots the percent degradation over this time period and suggests that wavelengths of light in the visible spectrum do little damage to solution-based TPB films. Indeed, plates exposed to light within the visible spectrum seem to have degraded by 15% at most over four weeks, while the full spectrum fluorescent light reduced TPB film performance by about 50% over that time. This result, combined with our conclusions from section 4, seems to suggest that light in the ultraviolet region plays the largest role in partially embedded TPB degradation. In particular, wavelengths longer than 700 nm are less likely to do harm than wavelengths shorter than 400 nm, due to their lower energies. This hypothesis was confirmed by testing plates with UV-blocking filters and observing a decrease in degradation similar to that seen when using any of the colored filters. We cannot rule out the possibility that visible light may have a small detrimental effect on TPB because of the small observed degradation. Another possibility is that UV light may have leaked through the low-wavelength cutoff of the colored filters.

6 UV-blocking materials as a preventative measure

6.1 Setup

Inferring that wavelengths in the UV spectrum are most likely the main cause of solution-based TPB film degradation, we looked to UV-blocking materials to mitigate the harm done. The two

2012 JINST 7 P07007

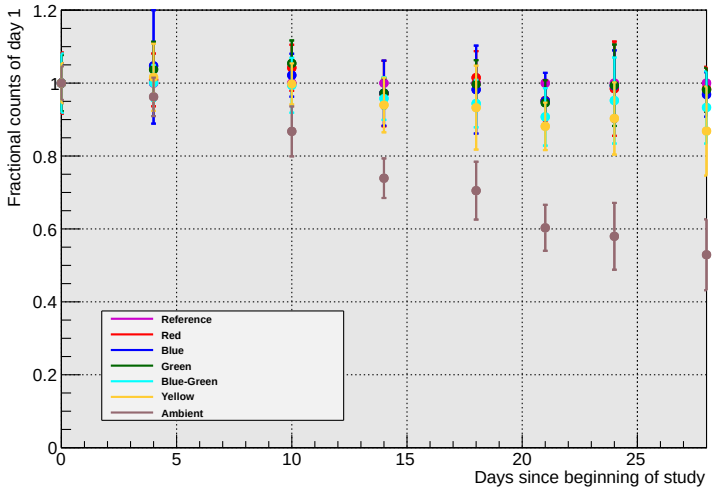

Figure 5. Fractional initial performance of TPB-coated plates placed under each type of filtered light, monitored over one month.

possible sources of UV light in our laboratory are the UV components of common fluorescent light and of ambient sunlight. We targeted each source separately: we used UV-blocking sheaths purchased from McMaster-Carr that fit over fluorescent lights, and we have found commercially available UV-blocking films for installation on our windows. The spectrum of each light source with and without each UV-blocker is shown in figure 6. We then examined the ability of each to reduce or prevent TPB degradation.

These preventative measures were evaluated separately for the fluorescent lights and sunlight. We monitored TPB degradation due to filtered and unfiltered sunlight without fluorescent lights, where plates were placed on the windowsill in direct sunlight. Similarly, we examined degradation due to filtered and unfiltered fluorescent lights with no ambient sunlight. Measurements to quantify performance were taken with the test stand described in section 3.2.

6.2 Results

For TPB-coated plates placed on a windowsill under direct sunlight and no fluorescent light, we noticed less degradation when the UV-blocking films were installed on the windows. After about 3.5 hours of exposure to these two conditions, we report about 15% degradation in filtered sunlight and 47% degradation in unfiltered sunlight. Thus, it seems that although the UV-blocking films did not completely stop partially embedded TPB degradation, they were very helpful in ameliorating the situation. We suspect that the magnitude of degradation from sunlight also depended on environmental factors such as time of day, season, and cloud cover. We note that, in general, plates should be stored out of direct sunlight, with or without UV filters.

A similar effect occurred for plates placed under fluorescent lights with and without the UV-blocking sheaths. After approximately 75.4 hours, plates under unfiltered fluorescents degraded by about 15%, whereas plates under filtered fluorescents degraded by about 4%. As with sunlight, we

2012 JINST 7 P07007

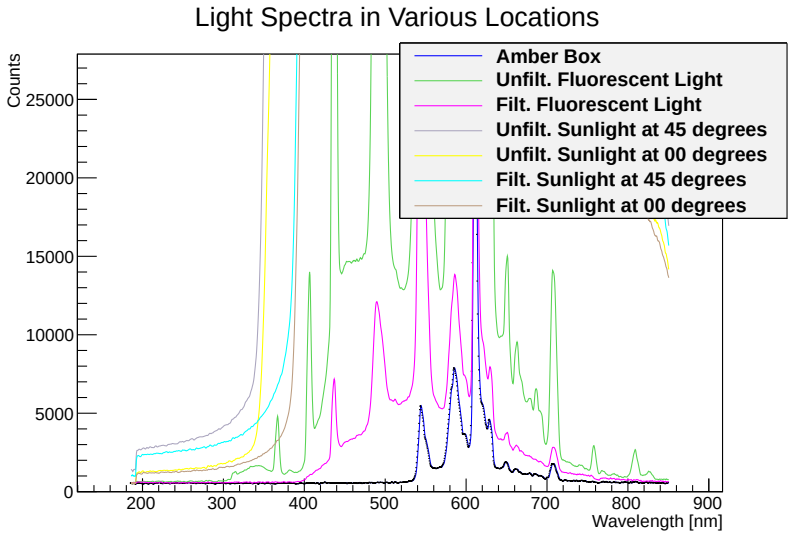

Figure 6. Light spectra of the light sources with and without UV blockers in place. Notice also that the viewing angle has a large effect on each spectrum. Because distance from the light source largely determines light intensity, the number of counts does not provide any useful information. Rather, we are simply interested in the cutoff wavelengths between 300 and 450 nm.

believe that proximity to the fluorescent light source influenced degradation as well. Indeed, we observed this to be the case in the colored filters study. From these results, it seems that the main culprit in our study from section 4 was the sunlight. We cannot draw any rigorous conclusions regarding the comparison between sunlight and fluorescent light because there are many unmeasured factors, such as plate location and angle with respect to each light source.

These results should be used only to compare degradation with and without each of the UV-blockers, and as general indicators of degradation. It is difficult to quantify exactly the amount or wavelength distribution of light reaching a TPB-coated plate placed in any given location in the lab. Not only can sunlight change unpredictably, but proximity and angle to light sources can drastically affect measurements between successive repetitions of this study.

7 Conclusion

We have demonstrated the harmful effect of certain wavelengths of light on the degradation of 50% TPB-PS chemical TPB coatings and isolated the most damaging wavelength range to the UV spectrum. On the other hand, we have seen that humidity does not play a significant role in long-run plate degradation. These effects have been seen only for films produced through TPB and PS dissolved in toluene, however we hypothesize that similar phenomena will occur for evaporative coatings.

Furthermore, we have determined that UV-blocking film ameliorates the damage from these wavelengths of light. Each of the two types of UV-blocker may reduce degradation by over two-thirds. However, because they cannot completely shield against degradation, we suggest that several other measures be taken to preserve these TPB-coated acrylic plates. First, they should always

2012 JINST 7 P07007

be kept out of direct sunlight. Second, although plates can be exposed to sunlight or fluorescent lights, this should only occur for about an hour at most to minimize any degradation. UV-blocking filters should be installed on windows and lights if possible. Finally, we recommend that although TPB films can be applied in a lighted environment, prepared plates should be stored in the dark until installation. With these precautionary measures, TPB can be used successfully as a wavelength shifter in LArTPCs.

Acknowledgments

The authors thank the National Science Foundation (grant number NSF-PHY-084784) and the Paul E. Gray Fund for the Undergraduate Research Opportunities Program at MIT.

References

[1] H. Chen et al., *Proposal for a new experiment using the Booster and NuMI neutrino beamlines: MicroBooNE*, FERMILAB-PROPOSAL-0974.

[2] ICARUS collaboration, S. Amerio et al., *Design, construction and tests of the ICARUS T600 detector*, *Nucl. Instrum. Meth.* **A 527** (2004) 329.

[3] ARGONEUT collaboration, C. Anderson et al., *First Measurements of Inclusive Muon Neutrino Charged Current Differential Cross Sections on Argon*, *Phys. Rev. Lett.* **108** (2012) 161802 [arXiv:1111.0103].

[4] LBNE collaboration, T. Akiri et al., *The 2010 Interim Report of the Long-Baseline Neutrino Experiment Collaboration Physics Working Groups*, arXiv:1110.6249.

[5] *MicroBooNE technical design report* (2011) .

[6] A. Hitachi et al., *Effect of ionization density on the time dependence of luminescence from liquid Ar and Xe*, *Phys. Rev. B.* **27** (1983) 5279.

[7] M. Antonello et al., *Analysis of liquid argon scintillation light signals with the Icarus t600 detector*, ICARUS-TM, 06-03 (2006).

[8] L. Bugel et al., *Demonstration of a Lightguide Detector for Liquid Argon TPCs*, *Nucl. Instrum. Meth.* **A 640** (2011) 69 [arXiv:1101.3013].

[9] V. Gehman et al., *Fluorescence Efficiency and Visible Re-emission Spectrum of Tetraphenyl Butadiene Films at Extreme Ultraviolet Wavelengths*, *Nucl. Instrum. Meth.* **A 654** (2011) 116 [arXiv:1104.3259].

[10] Eileen Hahn., private communication (2011).

2012 JINST 7 P07007

Appendix B

Benchmarking TPB Coatings

In addition to MicroBooNE itself, many other experiments are currently underway to develop the appropriate technology for large scale liquid argon time projection chambers. One of these involves the use of lightguides; this paper reports the results from several types of coatings on these lightguides as well as the behavior of the lightguides themselves.

My main contribution to this paper involves the creation of guidelines for proper lightguide storage in order to prevent TPB degradation. This includes the installation of UV blocking filters on the windows and lights of the laboratory where these measurements took place. This paper has been submitted for publication.

Preprint typeset in JINST style - HYPER VERSION

Benchmarking TPB-coated Light Guides for Liquid Argon TPC Light Detection Systems

B. Baptista[1], **L. Bugel**[2], **C. Chiu**[2], **J.M. Conrad**[2], **C.M.Ignarra**[2], **B.J.P. Jones**[2], **T. Katori**[2], **S. Mufson**[1]

[1]*Astronomy Dept., Indiana University, , Bloomington, Indiana, 47405*
[2]*Physics Dept., Massachusetts Institute of Technology, Cambridge, MA 02139*

ABSTRACT: Scintillation light from liquid argon is produced at 128 nm and thus must be shifted to visible wavelengths in light detection systems used for Liquid Argon Time Projection Chambers (LArTPCs). To date, designs have employed tetraphenyl butadiene (TPB) coatings on photomultiplier tubes (PMTs) or plates placed in front of the PMTs. Recently, a new approach using TPB-coated light guides was proposed. In this paper, we show that the response of lightguides coated with TPB in a UV Transmitting (UVT) acrylic matrix is very similar to that of a coating using a polystyrene (PS) matrix. We obtain a factor of three higher light yield than has been previously reported from lightguides. This paper provides information on the response of the lightguides so that these can be modeled in simulations for future LArTPCs. This paper also identifies areas of R&D for potential improvements in the lightguide response.

KEYWORDS: TPB, lightguide, Liquid Argon Time Projection Chamber, LArTPC.

Contents

1. Introduction

This paper discusses progress in the development of a lightguide-based system of light collection in liquid argon, primarily for use in a LArTPC experiment such as LAr1 [12] or LBNE [6]. Light collection systems exploit the fact that charged particles traversing liquid argon produce copious amounts of ultraviolet scintillation light. The scintillation photon yield is tens of thousands per

MeV of energy deposited [14], with depending on electric field, local ionization density and impurity concentrations at the parts-per-billion level.

The light has a wavelength of 128 nm and is produced via two distinct scintillation pathways with different time constants: a prompt component with lifetime of $\tau = 6$ ns and a slow component with $\tau = 1500$ ns [7]. An intermediate component with $\tau = 40$ ns has also been reported by some groups [4]. The relative normalization of early to late scintillation light depends upon the ionization density in the argon, and has been utilized as a particle identification variable in some dark matter searches [9].

This paper benchmarks improvements to a recently reported lightguide detector design for light collection in LArTPCs [10]. It also provides information that is useful for developing monte carlo simulations of lightguides, for development of future projects. In Sec. 2, we begin with a brief discussion of the motivation for light collection. Then, Sec. 3 provide the recipes for two coatings that have been studied. In Sec. 4, we describe characteristics of the acrylic bars used in this study. Next, in Sec. 5, we provide a description of the apparatus used to test the lightguide response, followed by a discussion of the waveform analysis (Sec. 6). Sec. 7 presents the study of the lightguide response, and lastly, Sec. 8 summarizes our results. Throughout the discussion, we identify points where further R&D are likely to produce substantial advances.

2. Light collection in LArTPCs

2.1 Liquid argon time projection chamber (LArTPC)

In development of LArTPC detectors, most of the attention has focused on collection of charge to reconstruct tracks to very high precision. When charged particles traverse the detector, ionization electrons are liberated from the argon atoms by particles traversing a body of liquid argon. These electrons are drifted by an electric field and measured with crossed wire planes to form a 3D image of the charge deposits left along the tracks of neutrino interaction products. The coordinates of the charge deposits perpendicular to the wire planes is obtained from the drift time for the ionization electrons to reach the wires. To obtain the absolute drift time, and hence the perpendicular coordinate of the event in the detector volume, the time that the primary interaction occurred, t_0, is used.

2.2 Motivation

Recently, attention has turned to establishing light collection systems. By collecting and measuring the argon scintillation light we can record the time structure of the event with few-nanosecond precision and determine the real t_0 of the event. This provides a method for establishing t_0 in cases where beam timing cannot be used. This is a much faster and more broadly applicable method than using the attenuation of charge of known MIP particles to establish the drift start-location.

We must know t_0 and hence the absolute drift distance for several important reasons. Firstly, liquid argon TPCs are commonly run in pulsed neutrino beams, with beam spills on the order of a microsecond. Surface based TPCs such as MicroBooNE and some LBNE options expect to be bombarded with a high rate of cosmic rays and secondary cosmogenic particles such as spallation neutrons which can mimic neutrino interactions. It is therefore vital to determine the interaction

time with microsecond precision to veto the events which occur outside of the beam window. Once it has been determined that an interaction occurred within the beam window, the TPC can be triggered and read out. The recorded TPC image will in general contain several interactions: some corresponding to cosmogenic particles and one being the neutrino event we are seeking. Determining which interaction corresponds to an incident neutrino involves utilizing geometrical information provided by the optical systems in combination with information about the event topology from the TPC. During charge drift, diffusion and recombination of the ionization charge will occur. Hence there are drift distance dependent corrections which must be made to correctly measure the dE/dx of a track. Assuming neutrino events from the beam can be identified, t_0 is known from the beam structure and the necessary corrections can be applied. However, for physics searches which involve events without a known time of arrival, such as proton decay and supernova neutrino searches, t_0 must be measured by the optical system in order to apply the required corrections and make an accurate track energy measurement.

Triggering on the information from the optical system has other practical benefits from a technical point of view. A typical TPC neutrino detector will have a tremendous amount of channels, and forming trigger logic on such a large set is a complicated procedure. In contrast, a PMT based optical system can achieve coverage of the volume with tens of elements, and forming a trigger becomes more straightforward. Finally, there are possible applications of the optical information for particle ID by pulse shape discrimination. The fast to slow scintillation yield ratio can reveal information about the local ionization of a track, which may be particularly helpful for performing particle ID on very short tracks where a TPC based dE/dx determination is either unreliable or impossible.

2.3 Light Collection Using PMTs

Cryogenic photomultiplier tubes (PMTs), which have a photocathode with platinum undercoating, can be used for light collection at LAr temperatures (87 K). However 128 nm scintillation light cannot penetrate any glass windows. Also, typical bi-alkali PMTs are only sensitive to visible light, not the 128 nm scintillation light from LAr. Therefore, in a PMT-based system, the light must be shifted to longer wavelengths.

The favored solution in LAr detectors for shifting the 128 nm light has been to use a tetraphenyl-butadiene (TPB) layer between the detector and the PMTs. This fluorescent wavelength-shifter absorbs in the UV and emits in the visible with a peak at 425 ± 20 nm [15], which is a favorable wavelength for detection by bi-alkali PMTs. Many detectors have used PMTs directly coated with TPB on windows, applied as either an evaporative coating (ICARUS [7]) or embedded within a polystyrene (PS) matrix (WArP [4]). The MicroBooNE design separates the coating from the PMT by applying a TPB-PS mixture to an acrylic plate positioned directly in front of the PMT.

Generally the light collection systems of the large active volume detectors have favored the use of large PMTs, such as the Hamamatsu 5912-02mod 8-inch PMT used in MicroBooNE [11], which are sparsely distributed for economic reasons. These tubes are located in the field-free region of the detectors, typically behind of the TPC anode wire planes.

2.4 Lightguides as an Alternative System

In Ref. [10], we presented the first detection of scintillation light in liquid argon using a lightguide

system. That paper discussed how coated acrylic bars, arranged side-by-side as a paddle, and bent to guide light adiabatically to a single 2 inch cryogenic PMT, could provide a flat-profile light detection system that could potentially be inserted into dead regions between LArTPC wire planes. This potentially could provide an economical light collection system to collect light, if the design is sufficiently efficient.

The lightguides utilized a TPB-based coating with an index of refraction that was chosen to match acrylic bars. Acrylic was chosen as the substrate because it is resilient to cryogenic cycling and can be easily bent to the required form. Some of the visible light that is emitted when UV photons hit the TPB coating will undergo total internal reflection because the acrylic has an index of refraction for blue light ($n = 1.49$) that is higher than that of liquid argon ($n = 1.23$) [20].

The reported guides used a polystyrene-TPB coating, as suggested in Ref. [16], mixed in a 3:1 mass ratio. The mixture was dissolved in toluene for application as a liquid. This was the highest mass ratio that could be achieved without the TPB crystallizing on the surface of the guide. Crystallization must be avoided in lightguide coatings because the white crystals cause absorption and scattering of visible light as it is reflected along the bars, reducing the attenuation length. With this design, we were able to demonstrate light collection, albeit with fairly low efficiency.

3. Lightguide Coatings

We use two coatings in this study. The first was the same coating as used the study of Ref. [10], called PS25%. The second coating is a new recipe using UVT acrylic, called UVT33%. We will show below that the responses of the two coatings are nearly equivalent, and so either can be used in future detector designs.

3.1 PS25% Coating

This coating consists of:

- 1:3 TPB:polystyrene ratio by mass
- 50 ml of toluene for every 1 g of polystyrene

This is the coating used for our first lightguides [10].

3.2 UVT33% Coating

This coating consists of:

- 1:2 TPB:acrylic ratio by mass
- 50 ml of toluene for every 1 g of acrylic
- 1:5 ethyl alcohol: toluene ratio in volume

This coating uses UVT acrylic and produces a clear, high quality coating for use on waveguides. The TPB and UVT pellets are first dissolved in the toluene, then the ethanol is added. The coating is applied to the acrylic guide in a single brush stroke. From the amount of solution used

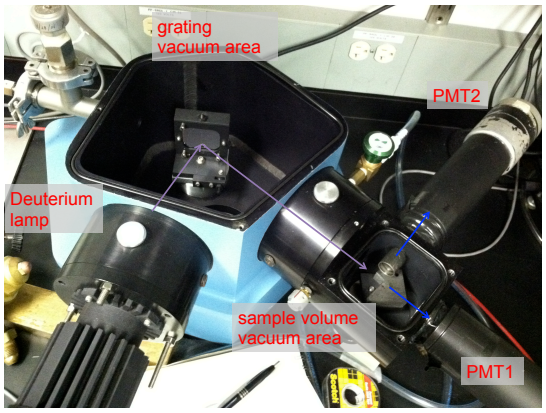

Figure 1. Setup for the vacuum monochrometer measurement. Light from the deuterium lamp enters a vacuum grating area where a specific wavelength can be selected by the grating to impinge on a sample. The emission from the sample can be observed by 2 PMTs located at built-in windows to the sample chamber. PMT 1 is used for this study.

to coat, we estimate approximately 5.5×10^{-5} g/cm^2 of TPB is deposited on the surface. However this cannot be related to the performance of the coated plate easily, because other factors, including coating method and surface condition, are equally important.

Addition of ethyl alcohol improves attenuation length because acrylic dissolved directly in toluene produces a rougher coating, more likely to scatter the light in the guides. Ethyl alcohol thins the coating as well as smoothing it. However, addition of ethyl alcohol may introduce negative effects, such as self-absorption. As we show later (Figure 3), the guided light at the TPB emission peak (436 nm) shows fairly uniform response against the incident spectrum. However, a few drops of ethyl alcohol introduces slight overall reduction ($<$10%) and a small dip at 270 nm. We have varied the fraction of alcohol to find the optimum ratio to Toluene.

3.3 Tests of Coatings in a Vacuum Monochrometer

Figure 1 shows the setup of the vacuum monochrometer test. Tests were performed in a McPherson 234 vacuum monochrometer using a McPherson model 632 UV Deuterium Lamp. Measurements were taken at a pressure of 11 ± 4 mTorr at room temperature, though results at 215 nm and 250 nm are consistent with measurements at atmospheric pressure. A PMT located outside of the vacuum region is used to see the forward emission of the sample plate. PMT 1 in figure 1 was used for this measurement.

The data in Figure 2 represent average measurements and are normalized with respect to average measurements of evaporatively coated plates. The evaporative samples contain pure TPB evaporated onto a plate in vacuum, and thus the effects of the different matrices can be compared to the pure TPB response. The evaporative samples used in this study have coating thicknesses of 1.87 μm. We expect these to be somewhat similar in performance to the plates used in reference [15], which had a thickness of 1.5 μm. The errors on each plate are associated with statistical errors including testing different samples of each coating type and systematic errors associated with the vacuum monochrometer. The overall efficiency including the error on the evaporative

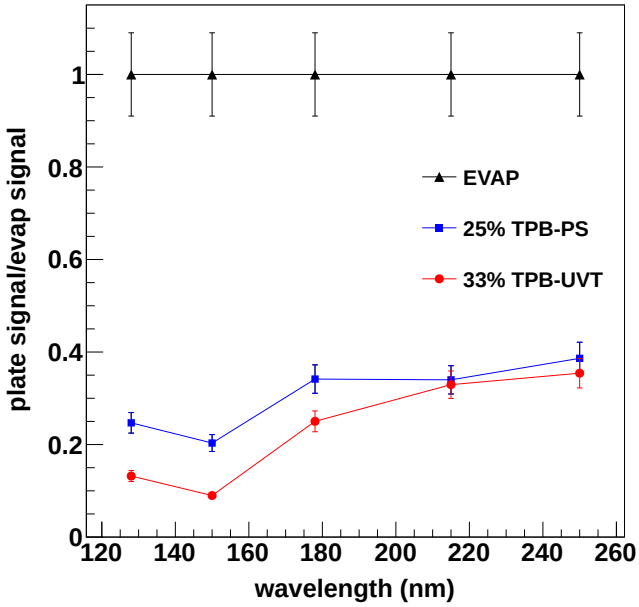

Figure 2. Coating efficiency as measured in a vacuum monochrometer as a function of wavelength. Samples are normalized to an evaporatively coated reference sample in order to calibrate out the spectrum of the Deuterium lamp. Error bars on the UVT and PS points only take into account the errors associated with these measurements, allowing for comparison between the two types of samples with each other, while error bars on the evaporative sample illustrate additional errors in the efficiency measurement.

measurement at 128 nm of our two types of coatings relative to the previously described evaporatively coated plates are 0.25 ± 0.03 and 0.13 ± 0.02 for the PS25% and UVT33% coated acrylic respectively.

These results on transmission of coated plates at room temperature are reproducible, as is reflected by the small errors. However, they contradict the results we will present in Sec. 7, where we will show very little difference in response between the PS25% and UVT33% coated lightguide performance in LAr. Indeed, in that section, we will show that UVT33% is slightly favored over PS25%. From this, we must conclude that either temperature plays an unexpected role in the relative emission between the two coatings, or that there is a difference in the capture efficiency between the coatings. The indices of refraction are 1.59 and 1.49 for the polystyrene and acrylic matrices, respectively, while the index of refraction of the cast bar is 1.49. Capture inefficiency could be exacerbated by the fact that the polystyrene has a smaller coefficient of expansion than the cast acrylic bar, while the acrylic coating and the bar are an exact match. So we suspect that the PS25% performance is degraded in the LAr, becoming very similar to the UVT33%. However, this is still under investigation.

3.4 Emission Spectra From Light Guides

The guided emission spectra from several short light guide segments of up to 10 cm in length

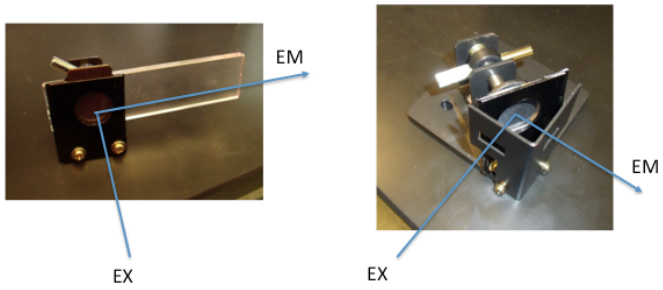

Figure 3. Spectrometer attachments used to obtain guided (left) and backward (right) emission and excitation spectra for lightguide sections.

were measured using a fluorimeter. A tunable monochromatic beam, produced using a grating and a xenon lamp, is normally incident upon the TPB coated surface of the light guide. The guided spectrum is measured at 90 degrees to the incident beam through of the end of the light guide using a second tunable grating and a photomultiplier tube. The spectrometer attachment used to implement this configuration is shown in figure 3 (left).

The lamp spectrum and PMT response are automatically accounted for by the spectrometer software, and the device is routinely re-calibrated using two standard samples : a rhodamine dye sample to characterize the emission grating and PMT response, and a diffuse glass cuvette to characterize the excitation grating and xenon lamp spectrum.

The guided spectrum was measured between 200 and 600 nm for incident wavelengths between 200 and 700nm. For segments of length 6 cm, 8cm and 10 cm, no differences in the shape of the emission or excitation spectra were seen. For incident light above 400 nm, no wavelength shifting behavior is observed, so we omit this region from the reported plots. Figure 4, top shows the two dimensional emission-excitation spectrum as a contour plot. We also show the emission spectrum at 250nm (Fig. 4, bottom left), and the wavelength shifting capability at the TPB emission peak wavelength of 436 nm (Fig. 4, bottom right). These one dimensional plots can be interpreted as a single horizontal and vertical slice from the two dimensional contour map, respectively.

The two dimensional excitation-emission spectrum for a backward emission was also measured. In this setup, a short light guide section is illuminated at 45 degrees to the surface with a monochromatic beam. The emitted light at 90 degrees to the incident beam is detected. The spectrometer attachment used to implement this arrangement is shown in figure 3 (right). The two dimensional backward excitation-emission spectrum for the light guide coating is shown in figure 5.

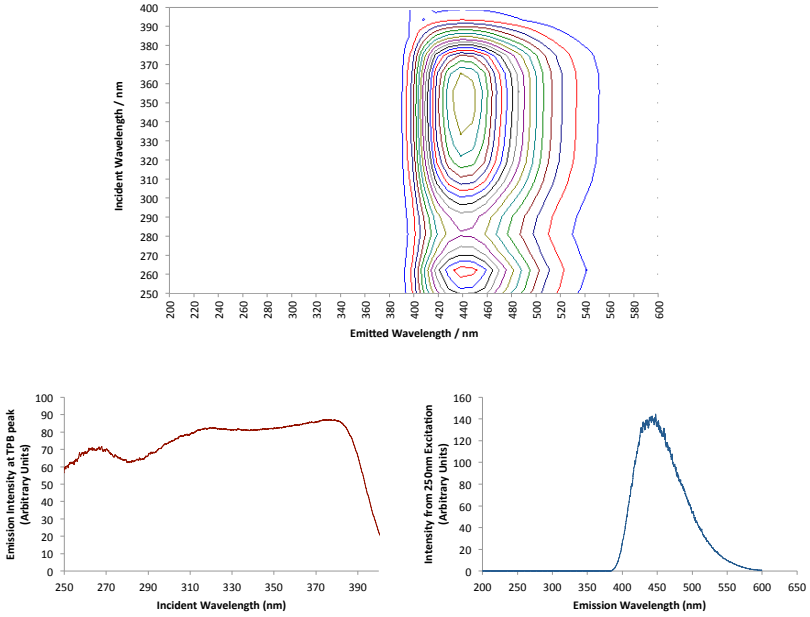

Figure 4. Emission and excitation spectra of wavelength shifted and guided light from a short light guide section with UVT33% coating. The top plot shows the two-dimensional emission excitation spectrum, bottom 2 plots are the slices of 436 nm emission (left) and 250 nm excitation (right).

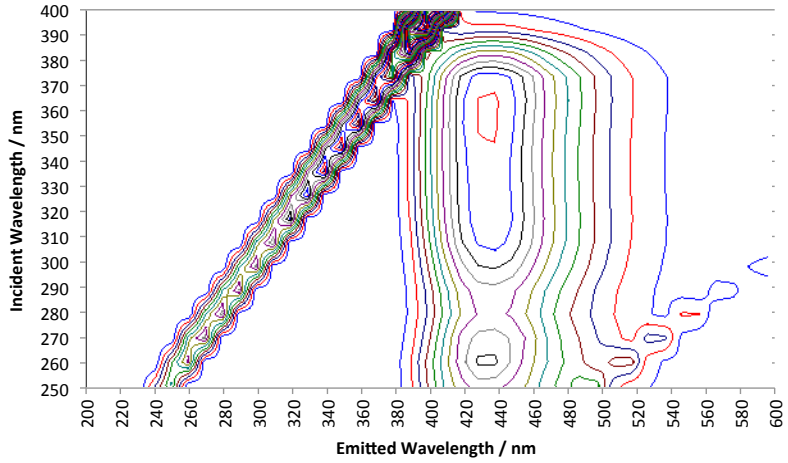

Figure 5. The two-dimensional backward emission and excitation spectra for the UVT33% and a thickly coated acrylic plate. The linear feature at EM=EX is directly reflected incident light. The second linear feature at lower wavelengths is a spectrometer alias due to the high intensity of direct light, and should be disregarded.

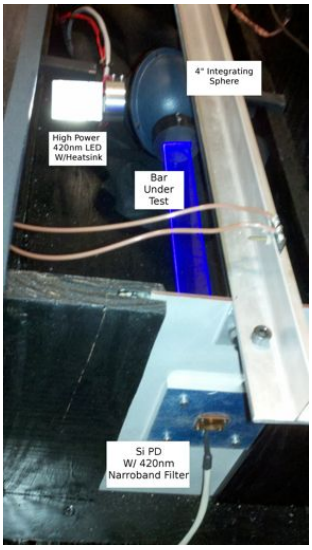

Figure 6. Setup used to measure the attenuation length of uncoated extruded acrylic and cast acrylic bars.

4. Bars Under Study

In the discussion below we consider coatings applied to extruded and cast acrylic bars to form light guides. Cast acrylic is taken to be the standard in our study. Our cast bars are purchased from Altec Plastics [19] and are polished on the ends. This replaces the extruded acrylic bars used in Ref. [10] purchased from McMaster-Carr [17] that are substantially more economical, however, have significant imperfections.

4.1 Attenuation Length Measurements of Uncoated Acrylic Bars

We measured the attenuation length of uncoated acrylic bars by illuminating the end of rods cut to various lengths and recorded the photo-current observed by a Si photodiode (PD). We used acrylic manufactured in two different ways: a cast UVA acrylic and an extruded UVA acrylic. The setup can be seen in figure 6.

The detector used to measure the light emerging from the end of the bars was an OSI Optoelectronics 3 mm Si PD (P/N: OSD15-0). In this configuration we are overfilling the detector and therefore only sampling a small fraction of the end of the bar. In addition, a 420 ± 10 nm narrow band filter was placed in front of the detector to restrict the attenuation length measurement to 420 nm. The illumination was performed with a high power 420 ± 10 nm LED (FutureLED P/N: FL-LED-440-420) driven at a constant current of 187 mA. The LED light was input into an integrating sphere to diffuse the light, thus illuminating the rod end with a uniform illumination pattern. The PD was mounted so that it views only the center of the bar through the narrow band filter. If the LED light is passed directly down the bar, the illumination pattern at the output of the bar is nonuniform and slight misalignments between the LED, light guide and PD can lead to systematics in the measurement of the attenuation length. Uniform illumination from an integrating sphere, on

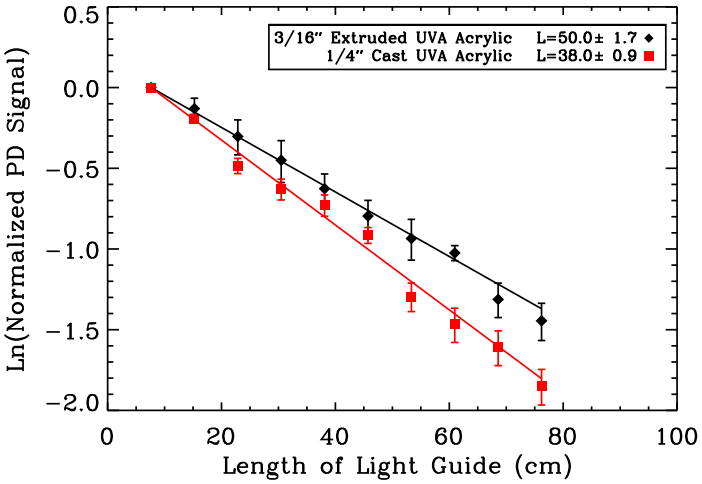

Figure 7. Attenuation length measurements of extruded and cast UVA acrylic bars at 420 nm. A fit to the data resulted in a measured attenuation length of 50±2 cm for the extruded UVA acrylic and 38±1 cm for cast UVA acrylic.

the other hand, will reduce this systematic significantly. This systematic would be minimized in a LAr detector design that under fills the PMT photo-cathode area.

Two sets of ten bars, one set for each type of acrylic, were measured with lengths increasing by 7.62 cm (3 inches) between 7.62 cm and 76.2 cm (30 inches). The 0.64×2.54 cm^2 (1/4 inch $\times$ 1 inch) cast UVA acrylic bars, purchased from Altec Plastics, were cut out of large acrylic 0.64 cm thick sheets. The cut edges on the 0.64×76.2 cm^2 face were polished by Altec Plastics using a polishing machine. The quality of measurement of attenuation length depends strongly on how well the sides are polished. The 0.48×2.54 cm^2 (3/16 inch $\times$ 1 inch) extruded UVA acrylic bar, purchased from McMaster-Carr, didn't require polishing on the 0.48×76.2 cm^2 face, because the bars were extruded at the 2.54 cm width and the factory edge was suitable for making this measurement. In both cases the ends of the bars were polished in the lab using a diamond tipped fly cutter after they were cut to length.

Fig. 7 shows natural log of the normalized photo-current versus the bar length for both the extruded and cast UVA acrylic. A fit to these data resulted in a measured attenuation length of 50±2 cm for the extruded UVA acrylic and 38±1 cm for cast UVA acrylic.

4.2 Preparation and Storage of Coated Bars

All bars used in the tests below are 60 cm in length and have polished ends. The cast bars are delivered with polished ends, while the ends of the extruded bars are polished in the lab. Before coating, bars are cleaned with ethyl alcohol. The coatings are applied with one brushstroke using an acid brush, depositing about 5.5×10^{-5} g/cm^2 of TPB

There is clear evidence that TPB coatings degrade with even modest exposure to laboratory fluorescent lights and sunlight [13]. Our studies show a 30% loss of response after a single day of exposure and 80% degradation after one month. Therefore the bars are handled in a laboratory

with UV filters installed on the fluorescent lights and windows. Furthermore, whenever possible, bars are kept covered with light-blocking cloths or are stored in opaque containers.

The previous study of lightguides predated the demonstration of the detrimental effect of UV light. Therefore, the precautions described above were not taken with the lightguides discussed in Ref. [10] . We think that this is the primary explanation for why the outputs of the PS25% lightguides presented in this paper are nearly a factor of three higher than that reported in Ref. [10].

There is some evidence that TPB coatings degrade by about 10% due to exposure to humidity in the laboratory [2]. This can be mitigated by desiccating the bars. The effect of humidity is relatively small and the evidence for improvement modest at best. Nevertheless, we store the bars used in these studies in containers with desiccant packets.

5. Apparatus for LAr Tests

The lightguide test stand was described in detail in Ref. [10]. The test stand is constructed from an open-top glass dewar which is 100 cm tall and 14 cm inner diameter into which a holder containing the lightguide is inserted. The holder has a 7725-mod Hamamatsu, 10-stage PMT [1] with a custom cryogenic base attached at the bottom. One PMT was used for all tests reported here. In the LAr, the PMT floats up against the lightguide which is fixed in the holder, making a good optical connection. An improvement to the holder of Ref. [10] guides the PMT so that the relative position between PMT face and bar is reproducible.

Lightguides are tested with 5.3 MeV α particles produced from a ^{210}Po source mounted in a plastic disk [18]. The source is electroplated onto foil that is recessed into a 3mm "well," of the plastic disk. In an improvement over Ref. [10], the disk is held in a holder with a 5.1 mm diameter hole, leading to a well of 4.8 mm depth. The αs emitted into the well traverse $\sim$50 μm in LAr. Scintillation light is then isotropically emitted. The well occludes most of the light; the solid angle acceptance for light at the bar is 7%.

The holder is immersed in LAr for 30 minutes before data is taken. Readout of the PMT is performed using an Alazar Tech ATS9870 digitizer. The Waveform is recorded on a scale of 200 mV/128 ADC counts and a trigger is produced by a negative pulse with an amplitude that exceeds 17 ADC counts, corresponding to a -27 mV threshold. When a trigger is produced, 128 pre-trigger samples and 384 post-trigger samples are recorded at a sampling rate of 1 giga-sample per second, leading to a total recorded profile of width 0.512 μs.

Triggers from the α source occurred at a rate of about 300 to 400 Hz, which was consistent with expectation given the short lifetime of the polonium. Runs were taken with no α source in order to measure the cosmic ray rate, which was found to be about 8 Hz. The dark rate, measured in runs with no light guide with the above threshold, was $<$1 Hz.

Our studies use four batches of industrial grade LAr. Industrial grade LAr is CGA certified to contain $<$20 ppm nitrogen and $<$ 5 ppm oxygen [8]. Running with "ultra-pure grade" which has has $<$5 ppm nitrogen and $<$ 1 ppm oxygen [8], was also an option, however we found no difference in the results of the studies below with the industrial versus pure LAr. This surprising result may arise for two reasons. First, the process of filling the open dewar system may lead to roughly equal contamination levels of the ultra-pure argon and the industrial argon. Second, the studies reported here focus on the quantity of early light, but not the quantity of late light. Impurities most

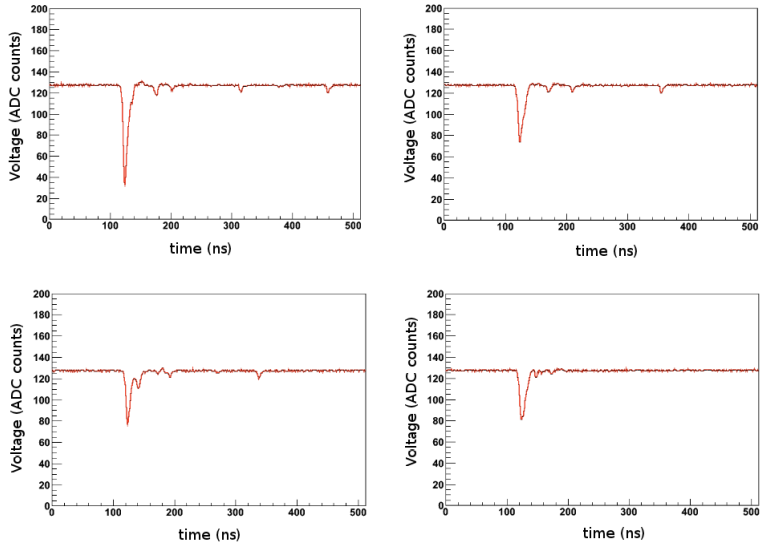

Figure 8. Four example events showing readout of waveform digitizer on a scale of ±200 mV/256 ADC counts. The scintillation light produced by the α has an early and late component. The triggering large pulse is primarily early light. The following small pulses are from single photons due to the late component.

dramatically affect the quantity of late light [3, 5]. With this said, further investigation with purified LAr is warranted.

In order to limit contamination by air when filling, the test stand is first filled with argon gas. The LAr is then poured through the gas into the dewar. We create the initial gas layer in the dewar by half-filling the warm dewar and allowing this LAr to evaporate.

6. Analysis of the Waveforms

Fig. 8 shows the waveforms of some example events from runs with the α source. One expects to see an initial peak corresponding to many photons followed by pulses from late light that correspond to a single UV photon hitting the bar distributed in time. The lifetime of the early light is 6 ns, and so one expects 95% of the photons to be produced within the first 18 ns of the pulse. In fact, the pulses appear somewhat wider due to fact that some late light also populates the initial peak, although this component is highly quenched due to the impurities in the LAr [3, 5]. As a result, the initial pulse is predominantly early light and we will refer to the initial pulse as early light in the discussion below.

6.1 The Pulse-finding Algorithm and Variables

We apply a pulse-finding algorithm that identifies pulses and records the maximum pulse-height from the baseline and the integrated charge of each pulse. The trigger is defined as when the signal drops to 17 or more ADC counts below the baseline. The pulse is then integrated from 30 ns before the trigger to 120 ns after the trigger. This defines total charge, Q_{tot}, which is our primary

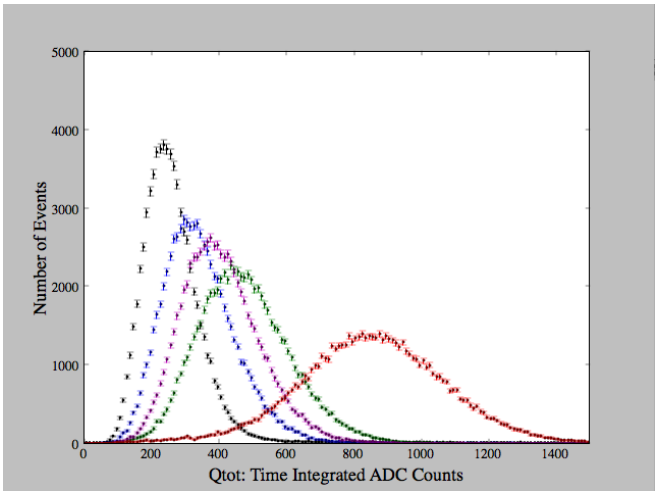

Figure 9. (color online). A variety of example Q_{tot} from cast acrylic bars with acrylic coatings with the source at 10 cm (black, narrowest distribution), 20 cm (magenta), 30 cm (green), 40 cm (blue) and 50 cm (red, widest distribution). The data are from four bars and four batches of LAr taken during a period of 60 days. All distributions have $> 70,000$ events.

observable. The long integration period accommodates large initial pulses from cosmic rays as well as the smaller initial pulses from the α source. The pulse-height, Q_{max}, is defined as the difference between the baseline and the minimum ADC count during the integration period. The baseline is recalculated using a 10 ns time window before each pulse, for both early and late light pulses. The start point for late light pulses is defined as when the signal drops to 2 or more ADC counts below the baseline.

6.2 The Q_{tot} Distributions of Early Light

After corrections for attenuation along the lightguide, the Q_{tot} distribution of the early pulses can be correlated to the energy of the α in the event. Examples of Q_{tot} distributions for the early light are shown in Fig. 9. One can see that the distributions form a Landau distribution. In the analysis below, we will study variations in these distributions as a function of position and batch of LAr. Thus, for illustrative purposes, we provide examples of distributions with the source at 10 cm (black), 20 cm (magenta), 30 cm (green), 40 cm (blue) and 50 cm (red) for various lightguides and LAr batches. In the analyses below, the Q_{tot} distributions are taken from runs of $> 70,000$ events.

Using Q_{tot} is a departure from the study in Ref. [10], which employed pulse-heights, Q_{max}. However, with the improved efficiency for the lightguides, we find that Q_{tot} is a better representation of the number of photons in an event. The issue arises when the photon arrivals are distributed over long time periods, leading to multiple peaks. An example of such a distortion is seen in the bottom left of Fig 8. This problem was addressed by the "multipeak analysis" of Ref. [10], however

employing Q_{tot} is a simpler and more accurate solution.

6.3 Late Light: A Single Photon Sample

As can be seen from Fig. 8, the late light is sparse, however the pulses are well-formed and uniform. The late light is particularly valuable, because it allows measurement of the Q_{tot} distribution for one and only one photon arriving at the PMT. Therefore, we utilize the late light to calibrate our system.

Our late light sample is acquired in the range > 400 ns after the initial pulse producing the trigger. This is sufficiently late in time that considering the yield and time constant of the light, we can be assured that the pulses which arrive at the lightguide correspond to only one UV photon. It has been shown that, on average, 1.3 visible photons are emitted from an evaporative TPB coating per one incident UV photon [15]; which is to say that occasionally TPB will produce multiple photons rather than one However, the acceptance of the lightguides, is only 5%, so there is a negligible probability of multiple photons arriving at the PMT.

Most methods of calibration, such as using low intensity LEDs, involve a Poisson distribution of photons arriving at the PMT which is then used to find the 1 PE response. In contrast, this calibration method is assured to sample exactly one photon hitting the PMT. As a result, one expects the Q_{tot} distribution of the late light will simply reflect the statistics of the early stages of the dynode chain, which is expected to be represented by a Gaussian to a good approximation [21]. As expected, the peak position varies with PMT voltage. However, for a given PMT, set at a specific voltage, the peak position is always located at 40 counts$\times$ns, regardless of the lightguide being tested. Also, we find that, for a specific lightguide-and-source set up, if the PMT high voltage is always adjusted such that the 1 PE response peak is at 40 counts$\times$ns, then the prompt light response is reproducible.

We demonstrate this in Fig. 10, where we overlay the late light distributions from five example runs. The examples cover four bars and four LAr batches and are typical of all the late light data sets. To allow comparison, the distributions are normalized in the range $Q_{tot} > 50$ counts$\times$ns, where background is expected to be low. One sees that the peaks of the late light are in good agreement, but the $Q_{tot} < 30$ counts$\times$ns can vary due to the relative strength of the background under the different environment. However this does not affect the location of the 1 PE peak, as Figure 10 show. The source of background is under investigation. The black squares show the mean of ten late light distributions.

Using the expectation for PMTs with large (> 4) secondary electron emission at the first dynode and high collection efficiency by the first few dynodes, we find a Gaussian fit to $Q_{tot} > 30$ counts$\times$ns yields a single PE peak at 39.3$\pm$1.0 counts$\times$ns. Thus, in the analysis that follows, the conversion from Q_{tot} to observed PE is obtained by dividing the results by 39.3 counts$\times$ns/PE. This was the same technique as was employed in Ref. [10].

7. Cast Acrylic Bars with Acrylic Coatings

The following tests are performed on cast acrylic light guides with UV33% coatings brushed onto cast acrylic bars.

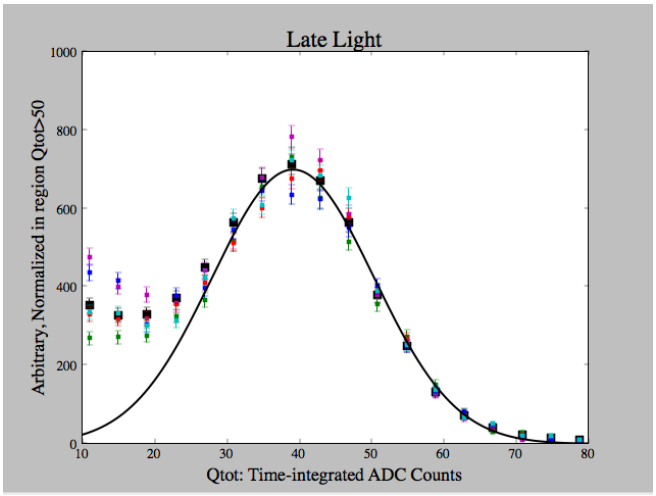

Figure 10. (color online). Colored symbols: Five example late light examples sampling all of the batches of LAr and bars and spanning the typical range of late light distributions. Samples were normalized in the range $Q_{tot} > 50$ counts$\times$ns. Black squares: mean of ten late light files, after normalization in the $Q_{tot} > 50$ counts$\times$ns range. The Gaussian is a fit to $Q_{tot} > 30$ counts$\times$ns.

7.1 Results of Tests in LAr

The studies presented here involve four batches of LAr and four bars, and were performed over about 60 days in order to study a variety of sources of variation of response.

Fig. 11 presents measurements for each of the four light guides under study, with a different symbol associated with each bar. The colors indicate the LAr batch in the test stand for a given measurement, where the time-order was: blue, red, magenta and green. Measurements are taken at up to five locations along the bar (10, 20, 30, 40 and 50 cm), and often multiple times. The source is removed and replaced between every measurement, even in the case where a measurement is taken multiple times at the same location. The exact location is varied within $\sim$ 1 cm. The purpose of this is to sample multiple areas of coating at each distance. Within a given location indicated on the plots, the measurements are presented in time order. Every measurement has more than 70,000 entries, and so the error bars are not visible on the plots.

Fig. 12 transfers information from Fig. 11, maintaining the meanings of the symbols for each bar and colors for each batch. In this figure, time information has been removed and the time integrated ADC counts, Q_{tot}, are plotted as a function of location of the source. The mean at each location is indicated by the black hexagon with the error bar. The deviation of measurements from the mean is such that a 16% systematic spread encompasses 68% of the data points.

The following conclusions can be drawn from Fig. 11 and Fig. 12:

- At a given source location, the spread of measured values is very large compared to the statistical error.

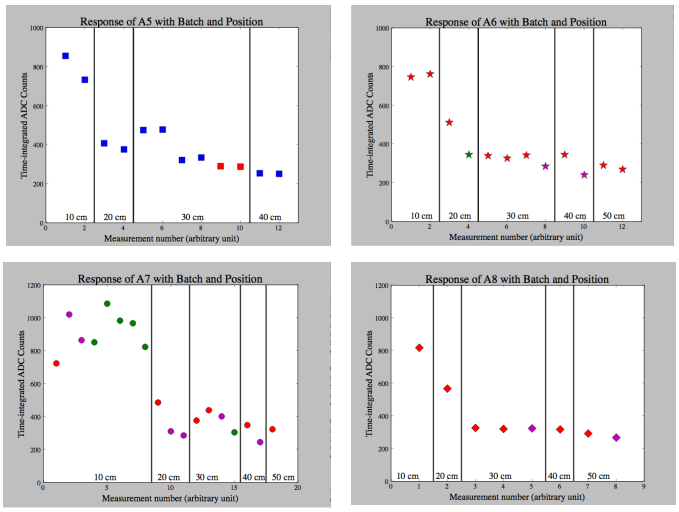

Figure 11. (color online). Plots corresponding to measurements of integrated charge, Q_{tot}, of early light for four lightguides. Measurements were made across four batches of LAr indicated by the color of the symbol. Measurements are made at multiple locations along a bar.

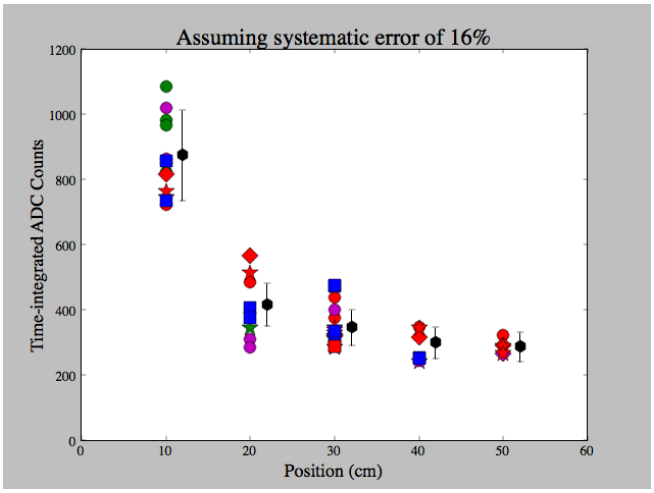

Figure 12. (color online). Q_{tot} as a function of position for four batches (colors) and four bars (symbols). Black hexagons indicate the average and error bars indicate a 16% systematic spread.

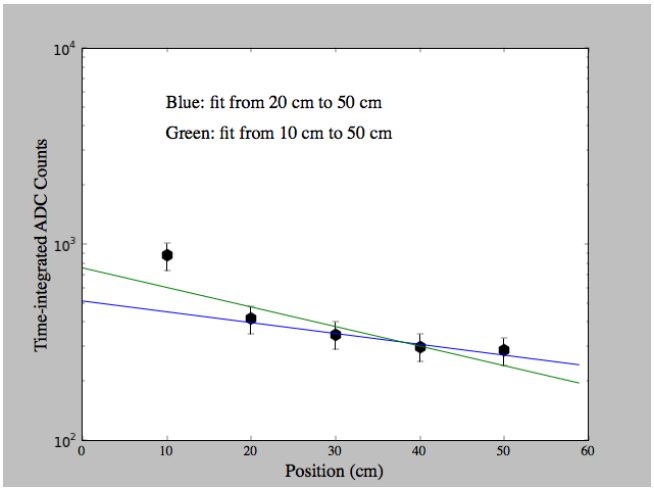

Figure 13. (color online). Exponential fits to the mean measurement at each position, taking the error to be 16%. The results at 10 cm are far from the expectation for an exponential, whether this point is included (green) or excluded (blue) in the fit.

- The spread in measurements at each location is, to a good approximation, the same fraction (16%) of the measured value.
- The spread is not due to LAr batch variations. The results from multiple batches are quite consistent within the spread.
- There is no evidence of systematic degradation with time due to an external source such as UV light.

The spread in measurements seems likely to be due to variations in the quality of the coating within the region sampled at each location.

In principle, one expects an exponential attenuation along the bar. Fig. 13 presents the mean of the measurements in LAr (black points) as a function of location along the bar on a semi-log plot. The point at 10 cm lies significantly higher than the expectation for an exponential. The green curve, which includes the 10 cm point in the fit, results in an attenuation length of 44 cm, while the blue curve, which excludes the 10 cm point, indicates an attenuation length of 79 cm.

These results are in qualitative agreement with the warm, uncoated acrylic bar measurements presented in Sec. 4.1), where the overall fit gave 38 ± 1 cm attenuation length. However, the warm, uncoated bars gave better agreement with a straight line on a semi-log plot. It is possible that the deviations observed in the LAr measurements come from the imperfections in coating. The source will be pursued in the future.

To establish the performance of the coating, apart from the attenuation, we use the 10 cm point as a benchmark. This is likely to be a conservative estimate as some attenuation may be occurring

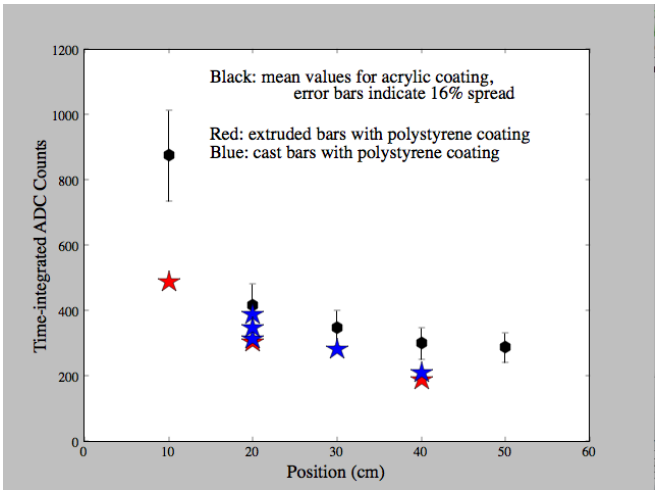

Figure 14. (color online). Comparison of LAr measurements for two coatings. Black circle: mean and spread of data from acrylic coating on cast acrylic bars. Red star: measurements on extruded bars with polystyrene coating. Blue star: measurements on cast bars with polystyrene coating.

over the 10 cm. The Q_{tot}-to-PE conversion yields 21.9 PE (7.2 PE) at 10 cm (50 cm). This result can be compared with the previously reported light guides that reported ~ 7 PE at 10 cm.

7.2 Comparison of Acrylic vs Polystyrene Coatings.

The cast bars with UVT33% coating are compared to cast bars and extruded bars with PS25% coating in Fig. 14. The acrylic coating is consistently better than the polystyrene coating by a factor of about 1.3.

8. Conclusions

This paper has presented information useful to simulating lightguide paddles in future LArTPC experiments. We have presented a comparison of response of lightguides prepared with two coatings, UVT33% and PS25%. We find that the response levels are similar for lightguides in LAr, although the transmission tests at room temperature indicated that PS25% was the better coating. At 10 cm, typical response of the light guides is about 21 PE, which is a factor of three improvement over previously reported lightguides.

Acknowledgments

The authors thank the National Science Foundation (NSF-PHY-084784) and Department Of Energy (DE-FG02-91ER40661). We thank Dr. A. Pla of Fermi National Accelerator Laboratory for helpful discussions and use of equipment.

References

[1] See http://sales.hamamatsu.com/index.php?id=13226699.

[2] The WArP Programme, 2008 Annual Report, preprint number LNGS-AR-2008-WArP.

[3] R. Acciarri et al. Effects of Nitrogen contamination in liquid Argon. *Nucl. Phys. Proc. Suppl.*, 197:70–73, 2009.

[4] R. Acciarri et al. Effects of Nitrogen contamination in liquid Argon. *JINST*, 5:P06003, 2010.

[5] R. Acciarri et al. Oxygen contamination in liquid Argon: combined effects on ionization electron charge and scintillation light. *JINST*, 5:P05003, 2010.

[6] T. Akiri and others [LBNE Collaboration]. The 2010 interim report of the long-baseline neutrino experiment collaboration physics working groups. arXiv:1110.6249 [hep-ex].

[7] M. Antonello et al. Analysis of liquid argon scintillation light signals with the icarus t600 detector. *ICARUS-TM*, 06-03, 2006.

[8] Compressed Gas Association. Commodity Specification for Argon. *G-11.1*, 2008. http://www.cganet.com/customer/publication_detail.aspx?id=G-11.1.

[9] M.G. Boulay. DEAP-3600 Dark Matter Search at SNOLAB. 2012.

[10] L. Bugel, J.M. Conrad, C. Ignarra, B.J.P. Jones, T. Katori, T. Smidt, and H.-K. Tanaka. Demonstration of a lightguide detector for liquid argon tpcs. *Nucl.Instrum.Meth.*, 640(1):69 – 75, 2011.

[11] H. Chen et al. Proposal for a New Experiment Using the Booster and NuMI Neutrino Beamlines: MicroBooNE. FERMILAB-PROPOSAL-0974.

[12] H. Chen et al. A LOI for a Neutrino Oscillation Experiment on the Booster Neutrino Beamline: LAr1. *Fermilab Letter of Intent*, P-1030, 2012.

[13] C. S. Chiu, C. Ignarra, L. Bugel, H. Chen, J. M. Conrad, B. J. P. Jones, T. Katori, and I. Moult. Environmental effects on tpb wavelength-shifting coatings. *Journal of Instrumentation*, 7(07):P07007, 2012.

[14] D. Gastler, E. Kearns, A. Hime, L.C. Stonehill, S. Seibert, et al. Measurement of scintillation efficiency for nuclear recoils in liquid argon. *Phys.Rev.*, C85:065811, 2012.

[15] V.M. Gehman, S.R. Seibert, K. Rielage, A. Hime, Y. Sun, et al. Fluorescence Efficiency and Visible Re-emission Spectrum of Tetraphenyl Butadiene Films at Extreme Ultraviolet Wavelengths. *Nucl.Instrum.Meth.*, A654:116–121, 2011.

[16] D.N. McKinsey et al. Flourescence Efficiencies of Thin Scintillating Films in the Extreme Ultraviolet Spectral Region. *NIM*, B132:351, 1997.

[17] McMaster-Carr. http://www.mcmaster.com.

[18] United Nuclear. http://www.unitednuclear.com.

[19] Altec Plastics. http://www.altecplastics.com.

[20] A. C. Sinnock and B. L. Smith. Refractive Indices of the Condensed Inert Gases. *Phys. Rev.*, 181:1297–1307, 1969.

[21] N. Tagg et al. Performance of Hamamatsu 64-anode photomultipliers for use with wavelength shifting optical fibres. *NIM*, A539:668, 2005.

Appendix C

MicroBooNE Vertical Slice Test

In addition to completing the two sets of measurements that were described in the body of this thesis, I studied many of the system's individual components. This includes the installation of a cosmic ray trigger so that cosmic events can be isolated and studied specifically. This appendix documents the trigger installation, LED characterization, preliminary late light quenching measurements, and an attempt to characterize and determine the cause of high frequency oscillations seen on our pulses. I contributed to each of these topics, and wrote this document as a technical report for the MicroBooNE collaboration.

MicroBooNE Vertical Slice Test

Christie Chiu, Ben Jones

August 16, 2012

Abstract

This document describes the various measurements and tasks that were completed over the course of Summer 2012 with the PMT side of the Bo Vertical Slice Test. These measurements include LED visibility studies, the installation of a cosmic ray trigger, late light studies, and 1 PE area measurement. We also describe noise in our signal and our attempts at eliminating it.

1 Apparatus and Setup

The MicroBooNE vertical slice test consists of a cryostat ("Bo"), which contains two MicroBooNE PMTs (#11 as PMT 1 and #16 as PMT 2) and two TPB-coated plates, one placed above each PMT. Two 95 Ohm high voltage cables connect the PMTs to high voltage feedthroughs located on the lid of Bo. Similarly, four quartz optical fibers lead from fixed positions within the cryostat to optical feedthroughs on the lid of Bo. The fiber locations are as follows:

UV 1 This fiber end points towards TPB plate 1, which is located in front of PMT 1. It is located approximately 25 cm from the plate surface.

UV 2 This fiber end points towards TPB plate 2, which is located in front of PMT 2. It is located approximately 25 cm from the plate surface.

VIS 1 This fiber end points towards PMT 1, and is located approximately 1 cm from the PMT surface.

VIS 2 This fiber end points towards PMT 2, and is located approximately 1 cm from the PMT surface.

A diagram of the setup is located in figure 1.

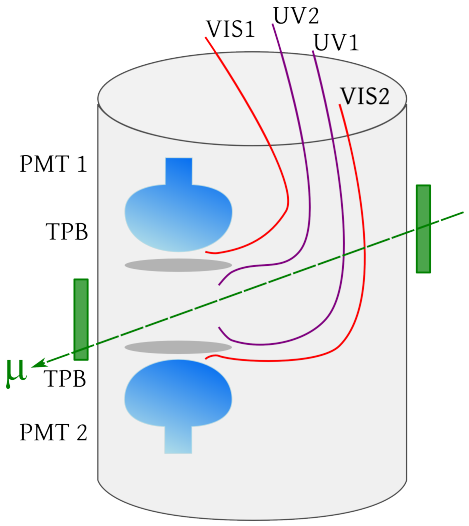

Figure 1: Cartoon depiction of setup with Bo, the cryostat detector used for the MicroBooNE Vertical Slice test.

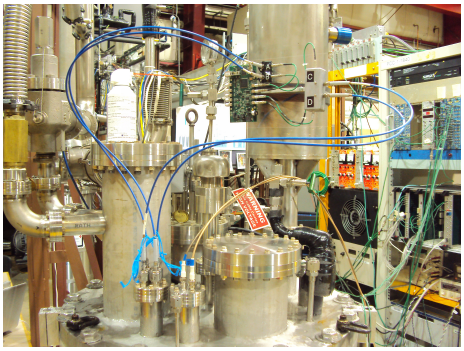

Figure 2: Photo of pulser board and LED installation.

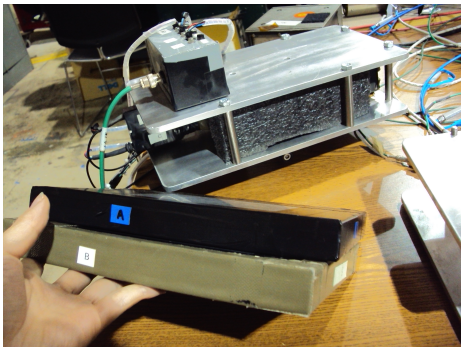

Figure 3: Photo of paddles used for the cosmic ray trigger, and the mechanical support for the paddle system.

The vertical slice test setup contains two UV and two visible LEDs which can be connected to any of the four optical fibers. These LEDs are controlled via a pulser board, which is programmed from a MicroBooNE server (uboonedaq02).

The cryostat also has a cosmic ray trigger, consisting of two scintillator paddles. Each paddle is placed on one side of Bo such that when a muon passes through both, it will pass through the LAr in the cryostat as well.

These components are connected via a schematic which can be found in slide 1 of document 2142 in the MicroBooNE DocDB. Slides 11 and 14 of this document also contain a more detailed description of the wiring involved for the cosmic ray trigger and pulser board.

More information about the pulser board and cosmic ray trigger setups can also be found below.

1.1 Pulser Board and LEDs

A photo of the pulser board and LED mount is in figure 2. It should be noted that LEDs A and B are blue LEDs, while LEDs C and D are UV LEDs of peak wavelength 270 nm. For these studies, LED D was broken and therefore only one UV LED was used.

For these measurements, when the pulser board was in use it was set to pulse at 100 Hz, in the pattern described in document 2043 of the MicroBooNE DocDB.

1.2 Cosmic RayTrigger

The cosmic ray paddles (figure 3) were previously constructed for the cryostat, and exist as two pairs of paddles. Each pair has a metal casing which can be attached to a vertical rod. The rod spans the height of Bo and affixes to the lid of Bo, such that each pair can slide up and down independently. Only one paddle in each pair is currently in use for the trigger, due to an insufficent number of logic gates (coincidence circuits) available.

The paddle signals are amplified and discriminated to reduce noise, then sent into a coincidence circuit (figure 4). Then, a trigger occurs whenever the paddles have a coincidence. The rate of accidental coincidences is very low, and is therefore negligible. An example of a cosmic muon trigger can be seen in figure 5; both the trigger and the PMT cosmic pulse can be seen. The rate of these triggers is very close to one per minute.

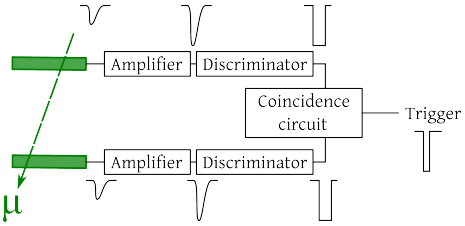

Figure 4: Schematic diagram of the cosmic ray trigger electronics.

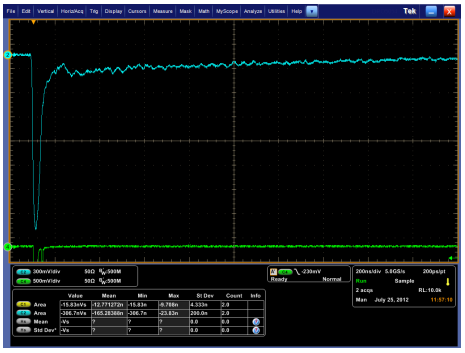

Figure 5: Demonstration of working cosmic trigger on scope. Trigger channel in green, PMT channel in blue.

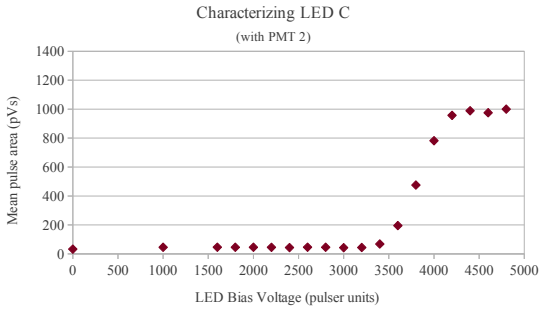

Figure 6: PMT 2 response to LED C (UV), with varying voltage to the LED. Voltage is expressed in LED voltage units.

2 LED Visibility

Thorough studies were performed to understand the visibility of UV and visible LEDs by the PMTs, with the LED light sent into one of the four fibers. This began with a characterization of each LED, as seen below.

2.1 LED characterization

To characterize each LED, it was first connected to its corresponding fiber. Then, for varying LED voltages, the PMT average peak area was measured. Both visible LEDs have already been characterized and LED D was broken, so only LED C was characterized. Figure 6 shows the mean pulse area for PMT2 taken while LED C sent UV light through the UV 2 fiber, and the voltage to LED C was set to values between 0 and 4800 voltage units. The trend in PMT response to varying LED voltage seems to be consistent with the characterization curves for the visible LEDs, which can be found in DocDB document 2043.

2.2 LED Visibility results: Round 1

Contrary to the description in section 1, round 1 of the LED visibility studies was performed

with a MicroBooNE spare PMT as PMT 1 and MicroBooNE PMT #11 as PMT 2. PMT 1 had a clear acrylic plate without TPB coating, while PMT 2 had an old TPB-coated acrylic plate.

Measurements were performed by connecting either a UV or visible LED to one of the fibers, then noting the subsequent response from one of the PMTs in terms of total pulse area. The compressed air duster was used before connecting any of the fibers to ensure a clean connection and increase repeatability of our results.

Visibility of visible LEDs to the PMTs was similar to those seen in document 2043 of the MicroBooNE DocDB. We noticed that these LEDs were only visible if the light was sent through fibers that pointed directly at the PMTs.

Visibility of the UV LED to PMT 2 was also as expected; the light was only detected when sent through the UV 2 fiber which pointed directly at the the TPB-coated plate above the PMT. However, visibility of the UV LED to PMT 1 was suprising. We expected it to always be invisible, regardless of fiber, because there was no TPB on the plate above PMT 1. Yet, PMT 1 saw UV light through UV 2 and VIS 1 (figure 7). The former could be explained by the fact that TPB re-emits light isotropically, so the UV light directed toward it was wavelength-shifted and a fraction of it was emitted towards PMT 1. As for the latter, we know that some PMTs are more sensitive to UV light than others, and this visibility could have been from that variation. We examined the interior of Bo after opening it for stray TPB, but found none, so it is unlikely that the detected UV light from VIS 1 had been wavelength-shifted.

2.3 LED Visibility results: Round 2

Round 2 of the LED visibility studies were performed with two MicroBooNE PMTs and two new TPB-coated acrylic plates, as stated in section 1. All other aspects of the study were the same.

We note that UV or visible light sent into each

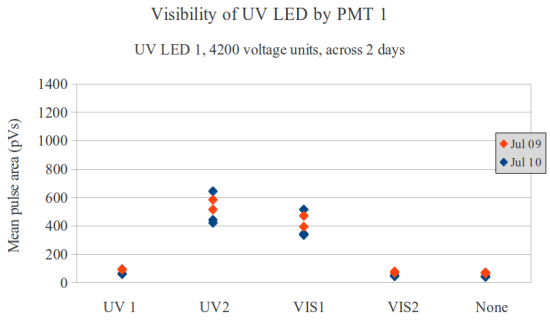

Figure 7: Visibility of UV and visible light to PMT 2, for light sent into each fiber individually.

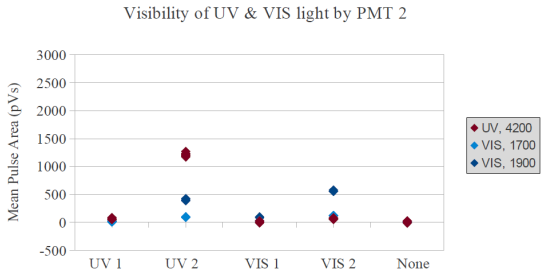

Figure 8: Visibility of UV and visible light to PMT 2, for light sent into each fiber individually.

of the four fibers in turn elicited the expected response from PMT 2 (figure 8). Indeed, it only saw visible light if it was sent into the VIS 2 or UV 2 fibers. Thus visible light pointed directly towards the PMT elicited a large pulse. Light pointed directly towards the plate above the PMT also reached the PMT, as the plate was not completely opaque. As for UV light, the PMT only saw it if it was directed towards the wavelength-shifting plate directly above the PMT.

With PMT 1, we had slightly more confusing results (figure 9). Visibility of both UV and visible light was as expected through fibers UV 2, VIS 1, and VIS 2, for the same reasons mentioned above. However, it seemed that UV or visible light sent though fiber UV 1 was invisible to PMT 1. The most logical explanation for

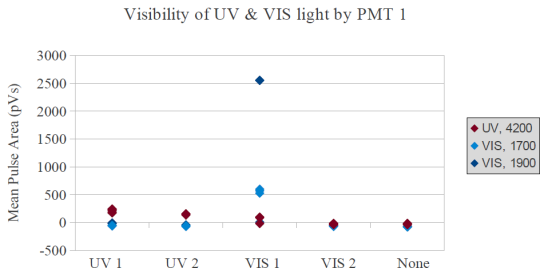

Figure 9: Visibility of UV and visible light to PMT 1, for light sent into each fiber individually.

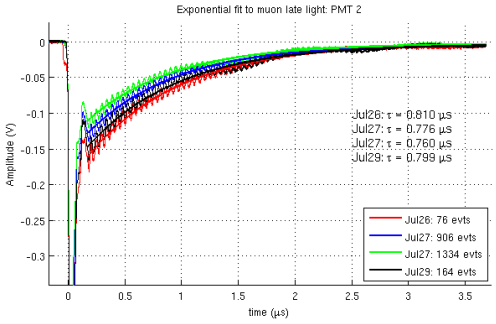

Figure 10: Many cosmic muon PMT pulses were averaged, and exponentials were fit to the late light tails. Data was taken every few days.

this was that the UV 1 fiber was not working. This could have been from a loose connection or from too much bending in the fiber. Indeed, UV 1 bended the most out of the four fibers in the system.

2.4 Light source stability

The stability of our LED source was also monitored. Figure 7 contains data taken over several repetitions and over the course of two days; all of these measurements seem to be consistent with each other, with high stability. Similarly, measurements taken with PMT 2 seem to be very stable.

3 Cosmic Ray Muon Measurements

Several measurements were taken using cosmic ray muon data, to demonstrate our understanding of the vertical slice test system. These included the measurement of the late light time constant, and the percentage of total scintillation light that is late light. We also measured the PMT signal when the paddles are moved so that the trigger did not correspond to cosmics traveling through Bo; this was our "randoms" measurement.

3.1 Late light time constant

Impurities in liquid argon seem to decrease the amount of late light received, thereby effectively decreasing the late light time constant. We sought to demonstrate this effect by monitoring the late light time constant with decreasing liquid argon impurity.

To do this, we used the cosmic ray trigger and measured the average of many cosmic ray pulses. Then an exponential was fit to the tail of this pulse. Ideally this would have been repeated once a day for both PMTs, over the course of several days, following a fresh fill of liquid argon. However, for this round our measurements were taken after the LAr had been sitting for a few days already, and the level was too low for operation of PMT 1. Our results can be seen in figure 10 for cosmics seen by PMT 2.

Notice that the noise in our signal affects the exponential fit; for more on the noise, see section 6. This noise needs to be reduced as much as possible or eliminated completely for greater accuracy on these fits.

Additionally, measurements should be taken after a fresh fill of argon and with both PMTs when possible. This may have to wait until oxygen and purity monitors are installed so that we have an absolute scale to compare against.

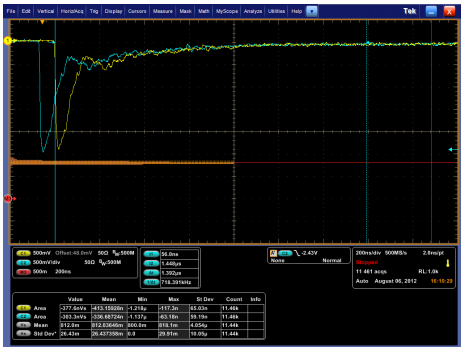

Figure 11: Scope screenshot of late light percentage measurement. PMT signal in blue, delayed PMT signal in yellow, and measurement window bounded by blue vertical lines (one solid, one dotted).

3.2 Late light percentage of total scintillation light

The percentage of total scintillation light that is comprised of late light can also be measured. This is particularly interesting because the percentage varies with the type of particle creating the scintillation light. For example, muons create scintillation light where about 77% is late light, while protons have a smaller percentage composed of late light.

We made this measurement by splitting a PMT signal and sending half directly into the scope. The other half was delayed with a 50 ft cable, equating to 75 ns of delay. This allowed us to measure the pulse area of both signals in a single common window. The window lined up with the entire pulse- prompt and late light- for the delayed pulse, and only the late light portion of the pulse without delay. The ratio of these areas, then, was histogrammed to give us the late light fraction distribution. See figure 11 for an oscilloscope screenshot of this setup.

One measurement was performed in this way, and yielded a single narrow peak at 81.2%. This was a reasonable percentage, however the peak was much narrower than we would have expected given all of the noise in our signal. Therefore, this measurement should be repeated once the noise is eliminated.

3.3 Measurement of randoms

We relocated the cosmic ray trigger paddles so that they were in the same location relative to each other and to the ground, but so that a muon travelling through both paddles would not also travel through Bo. This gave us a similar trigger frequency, but no corresponding muon event in our cryostat.

Then, measuring the PMT pulses from these triggers, we saw a very flat signal, with any noise averaging to the zero baseline over time. This indicated that there was no inherent noise in our system correlated with our cosmic ray trigger firing.

4 TPB-coated plates

There will be a separate document written to document the procedure for making plates and storing them. For these studies, two new TPB-coated plates were made. They were placed in the dark right after creation, and kept in the dark until installation. After installation, the plates were kept covered to the best of our ability, uncovered only right before Bo was sealed.

5 1 PE = 20 ADC calibration

A 1 PE = 20 ADC calibration involves measuring 1 PE pulses with the electronics rack and adjusting the PMT voltage such that a 1 PE pulse corresponds to a pulse height of 20 ADC from the electronics. To prepare for this calibration on the PMT side, the height and area of 1 PE was measured on the oscilloscope. This was done in two methods: using a visible LED with the pulser board at a very low LED voltage, and using single photons from the very end of late light.

Figure 12: We measure a 1 PE area in pVs on the scope by histogramming the pulse areas of pulses in response to a weak LED.

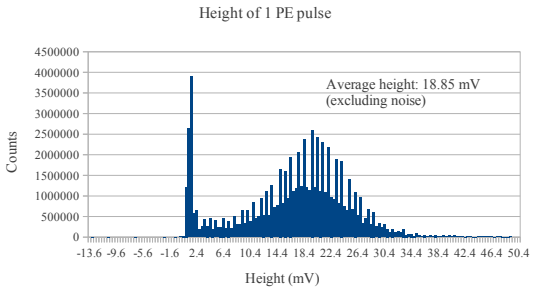

Figure 13: We measure a 1 PE height in mV on the scope by histogramming the peak heights of pulses located 3 μs after a cosmic prompt light pulse.

Using a visible LED connected to VIS 2, we histogrammed pulse areas for the pulses from PMT 2. As seen in figure 12, the histogram gives us a noise peak, a 1 PE peak, and a 2 PE peak. The center of the 1 PE peak then gives us the 1 PE area.

Using the late light tail of cosmics, we histogrammed pulse heights for the pulses seen between 3 μs and 5 μs after the prompt light pulse. The histogram (figure 13 gives us a noise peak and a 1 PE peak.

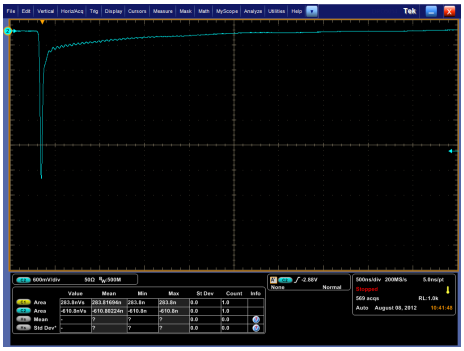

Figure 14: The reflection seems to disappear when impedance matching is satisfied.

6 Noise in PMT signal

In our measurements, we noticed three types of noise in our PMT signal, all of which occur only after a PMT pulse. Crucially, each type of noise occurs in the same phase across PMT pulses, and so they cannot be eliminated via averaging many pulses. They are as follows:

- One big reflection right after the PMT pulse
- High frequency ringing
- Low frequency ringing

All three can be seen very clearly in 10. We address each of these issues in turn.

6.1 Reflection

The reflection was resolved by sending the PMT signal directly into the scope, without being split to the electronics rack (figure 14. This lead us to believe that the cause of the reflection was simply due to an impedance mismatch; thus the reflection should be resolved when all components are adjusted for impedance matching.

6.2 High frequency ringing

An analysis of the high frequency ringing was performed by taking a fourier transform of the signal, as seen in figure 15. From this, we saw

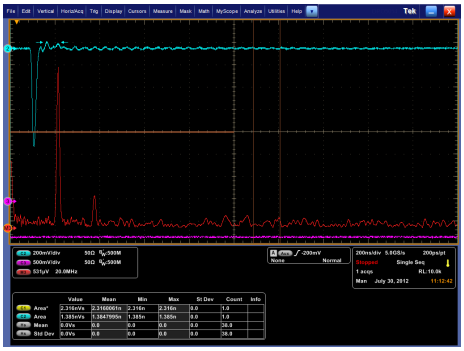

Figure 15: A fourier transform of the PMT pulse noise reveals frequency components at 21.5 MHz and 37.7 MHz.

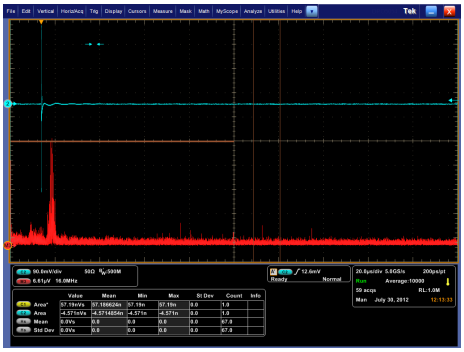

Figure 16: Driving the splitter, we see high frequency noise of the same frequency components as was in the PMT pulse noise.

that it has two frequency components: a larger one at 21.5 MHz, and a smaller one at 37.7 MHz.

There were only two components between the PMT and scope: the PMT base and the splitter. Thinking that the splitter may be the source of noise, we drove it with the pulser board signal (essentially a delta function) and observed the output on the scope. In other words, the HV input of the splitter was left open, while the anode was connected to the scope (as usual), and a delta function was sent in where the PMT is usually connected.

Doing this yielded a signal with the same high frequency noise that was seen in our PMT signal, with frequencies at 21.5 MHz and 37.7 MHz (figure 16).

Therefore, we performed the same measurement with a different splitter. This one was borrowed from the Solid Xe group, and had a slightly different circuit. It was also on a PCB, and therefore had no free wires as our box splitter did. Figure 17 shows the result; notice that there is no ringing.

Yet, using this splitter in our setup, we still observed high frequency noise after PMT pulses (figure 18). This suggests that there may be other sources of noise in the system which have the same frequency components.

We noticed that other similar setups (namely, Paul Nienaber's setup) did not have these fre-

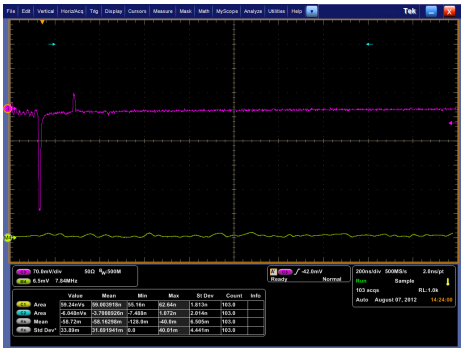

Figure 17: Driving the PCB splitter, we did not see any high frequency noise.

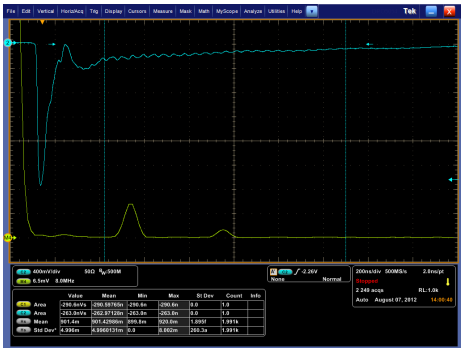

Figure 18: Driving the PCB splitter, we do not see any high frequency noise.

quency components of noise, which lead us to believe that it was a difference in these setups that caused the noise. Our setups have had the same PMTs and bases, differing only in HV source and splitter. We will try a different high voltage source to see if this eliminates our noise.

6.3 Low frequency ringing

This ringing had a frequency of approximately 1 MHz, and became most dominant at the end of the late light tail of a cosmic ray muon event, about 1.3 μs after the prompt light pulse. Unfortunately the source of this noise has not been determined yet. Because this noise affects our ability to perform late light exponential fits, eliminating it is of high priority.

7 Conclusion

The MicroBooNE Vertical Slice Test seems to be progressing nicely, with the installation of the cosmic ray trigger and ensuing measurements involving scintillation light.

The next time that Bo is opened, fiber UV 1 should be examined for a loose feedthrough connection or strong bending which may prevent the transmittion of light through it. Then, the tests should be repeated to determine whether this resolves the unexpected results from Round 2 of the LED visibility tests.

The biggest issue at this point is the noise on our PMT signals, and should be high priority to resolve. Once that happens, we should be able to begin taking useful measurements of the late light time constant and late light percentage of total scintillation light.

Bibliography

[1] S. Amerio et al. ICARUS collaboration. Design, construction and tests of the ICARUS T600 detector. *Nucl. Instrum. Meth.*, A 527:329, 2004.

[2] C. Anderson et al. ArgoNeuT collaboration. First measurements of inclusive muon neutrino charged current differential cross sections on argon. *Phys. Rev. Lett.*, 108:161802, 2012. arXiv:1111.0103.

[3] WArP Collaboration. Effects of nitrogen contamination in liquid argon. *JINST*, 5, June 2010.

[4] Wolfgang Pauli. Letter to L. Meitner. Pauli letter collection. Translation by K. Riesselmann, URL: http://microboone-docdb.fnal.gov/cgi-bin/RetrieveFile?docid=953;filename=pauli, 1956.

[5] Y. Grossman. Tasi 2002 lectures on neutrinos. arXiv:hep-ph/0305245v1, 2002.

[6] J. Beringer et al. (Particle Data Group). *Phys. Rev. D.*, 86:010001, 2012. URL: http://pdg.lbl.gov.

[7] A. Hitachi et al. Effect of ionization density on the time dependence of luminescence from liquid Ar and Xe. *Phys. Rev. B.*, 27:5279, 1983.

[8] Jr. K. Wark. *Advanced Thermodynamics for Engineers*. McGraw-Hill Series in Mechanical Engineering. McGraw-Hill Education, 1 September 1995.

[9] Wolfram|Alpha knowledgebase, 2013. www.wolframalpha.com.

[10] F. Cavanna. Some considerations on the intermediate component. 2008. Private communication.

[11] J.M. Conrad et al. Sterile neutrino fits to short-baseline neutrino oscillation measurements. *Advances in High Energy Physics*, 163897, 2013. URL: http://dx.doi.org/10.1155/2013/163897.